

Review

High-Performance Supercapacitors: A Comprehensive Review on Paradigm Shift of Conventional Energy Storage Devices

K. C. Seetha Lakshmi ^{1,*}, [†] and Balaraman Vedhanarayanan ^{2,*}, [†]

¹ Department of Chemistry, Graduate School of Science, Chiba University, 1-33 Yayoi-Cho, Inage-Ku, Chiba 263-8522, Japan

² Department of Applied Chemistry and Biotechnology, Graduate School of Engineering, Chiba University, 1-33 Yayoi-Cho, Inage-Ku, Chiba 263-8522, Japan

* Correspondence: seethakc@gmail.com (K.C.S.L.); bvedhanarayanan@gmail.com (B.V.)

† These authors contributed equally to this work.

Abstract: The enormous demand for energy due to rapid technological developments pushes mankind to the limits in the exploration of high-performance energy devices. Among the two major energy storage devices (capacitors and batteries), electrochemical capacitors (known as ‘Supercapacitors’) play a crucial role in the storage and supply of conserved energy from various sustainable sources. The high power density and the ultra-high cyclic stability are the attractive characteristics of supercapacitors. However, the low energy density is a major downside of them, which is also responsible for the extensive research in this field to help the charge storage capabilities thrive to their limits. Discoveries of electrical double-layer formation, pseudocapacitive and intercalation-type (battery-type) behaviors drastically improved the electrochemical performances of supercapacitors. The introduction of nanostructured active materials (carbon-/metal-/redox-active-polymer/metal-organic/covalent-organic framework-based electrode materials), electrolytes (conventional aqueous and unconventional systems) with superior electrochemical stability and unprecedented device architectures further boosted their charge storage characteristics. In addition, the detailed investigations of the various processes at the electrode–electrolyte interfaces enable us to reinforce the present techniques and the approaches toward high-performance and next-generation supercapacitors. In this review, the fundamental concepts of the supercapacitor device in terms of components, assembly, evaluation, charge storage mechanism, and advanced properties are comprehensively discussed with representative examples.

Keywords: energy storage; supercapacitors; electrodes; electrolytes; electrical double-layer capacitance; pseudocapacitance; battery-type material



Citation: Lakshmi, K.C.S.;
Vedhanarayanan, B.
High-Performance Supercapacitors:
A Comprehensive Review on
Paradigm Shift of Conventional
Energy Storage Devices. *Batteries*
2023, *9*, 202. <https://doi.org/10.3390/batteries9040202>

Academic Editor: George
Zheng Chen

Received: 28 January 2023
Revised: 22 March 2023
Accepted: 24 March 2023
Published: 29 March 2023



Copyright: © 2023 by the authors.
Licensee MDPI, Basel, Switzerland.
This article is an open access article
distributed under the terms and
conditions of the Creative Commons
Attribution (CC BY) license (<https://creativecommons.org/licenses/by/4.0/>).

1. Introduction

Energy storage devices are inevitable candidates in the field of energy preservation and its utilization. In general, the four types of energy storage through mechanical, electrical, chemical, and electrochemical systems have been employed for various applications, including large-scale energy conservation [1]. Among them, electrochemical energy storage with the help of capacitors and batteries plays a significant role, especially in electric vehicles and portable electronics. Electrochemical capacitors (supercapacitors) have grasped more attention due to their higher power density and ultra-cyclic stability [2]. In the middle of the 18th century, the concept of electrical double layer (EDL) structure and the formation of electrical potential at the solid–electrolyte interface were put forward by H. von Helmholtz, which seeded the fundamentals of the charge storage mechanism and the electrical double layer capacitance (EDLC) [3]. After hardly a century, the EDLC and the charge–discharge processes were demonstrated in an experimental electrochemical cell constructed by H. I. Becker for the ‘General Electrical Company’ [4]. It led to the first commercial supercapacitor based on EDLC by Ohio state’s Standard Oil Company, and it was subsequently licensed to

the Nippon Electrical Corporation (NEC) in 1971 for computer technology [5]. The term ‘Supercapacitor’ was first coined by the NEC, and the corporation also marketed the device in the name as well. Afterward, the term ‘Supercapacitor’ became familiar in Asia. Shortly, in 1982, the ‘Pinnacle Research Institute’ (PRI) developed a high-power electrochemical cell based on ruthenium oxide and commercialized it under the name of ‘PRI ultracapacitor’ that popularized the alternate term ‘ultracapacitor’ in North America [6]. In the past several decades, electrochemical energy storage systems have evolved with enormous growth by introducing new concepts of pseudocapacitance [7], battery-type behavior [8], and asymmetric and hybrid device [9,10] architectures towards high-performance and next-generation energy storage devices (Figure 1).

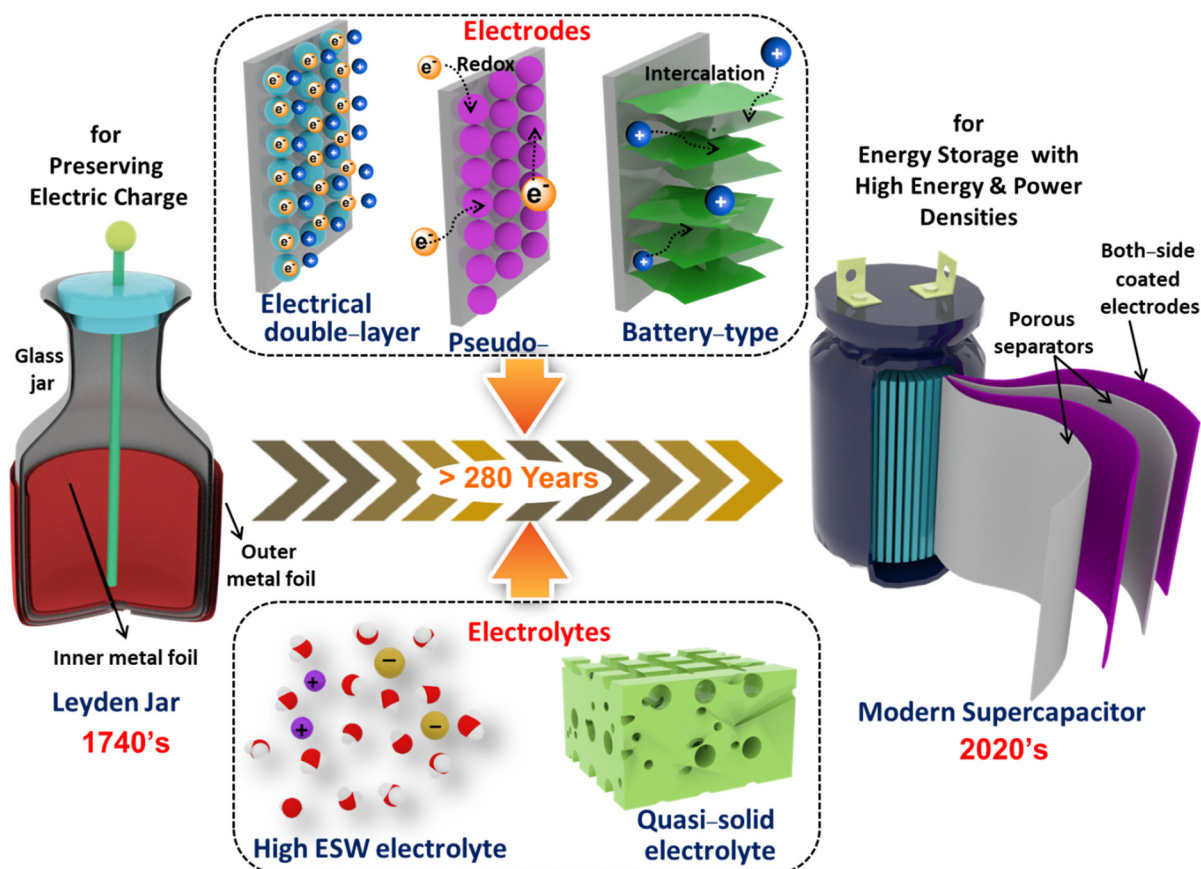


Figure 1. Schematic representation showing the evolution of modern supercapacitor devices through the various developments in their potential components.

Vast efforts have been invested to improve the performances of the supercapacitors by the proper materials design and device configurations [11]. The development of high-performing electrode and electrolyte materials is crucial to achieving improved electrochemical energy storage. The introduction of multi-role nanostructured materials has enormously boosted the electrochemical performances of supercapacitors [12]. Furthermore, the energy density/specific energy (the amount of energy stored by a unit volume/mass of the electrode material) of the supercapacitor ($<30 \text{ Wh L}^{-1}$), which is usually inferior to that of batteries ($\sim 500 \text{ Wh L}^{-1}$), is often increased by utilizing the electrolytes that can operate in wider potential window [1]. The ionic liquids and the unconventional electrolytes (water-in-salt (WIS) and deep-eutectic solvents (DES)) are examples of higher-performing electrolyte systems for supercapacitors [13]. The growth of sophisticated electrochemical characterization techniques resulted in an in-depth understanding of various aspects of the charge storage mechanism and electrode–electrolyte kinetics [14]. In this review, a systematic discussion of the fundamentals and developments in the field of

supercapacitors, including electrode kinetics, will comprehensively be covered. This review aims to provide a compact rundown of the various concepts of supercapacitors, especially for the benefit of young researchers, while detailed reviews on each topic are documented in the literature. We have cited those reviews in the respective sections, which would give the scope of in-depth understanding. The discussions of the present review are divided into five sections except for the introduction part. In Section 2, the basic components of a typical supercapacitor device, such as electrode materials, binder and conductive additives, current collectors, electrolytes, and separators, are summarily discussed. The majorly utilized electrode materials (synthesis and physicochemical properties) are generally categorized into five sub-sections: carbon-based, transition-metal compounds, two-dimensional (2D) layered materials, metal-organic, and covalent-organic frameworks. Furthermore, the electrolyte systems are grouped into three sub-sections: conventional aqueous, conventional nonaqueous, and unconventional electrolytes. Section 3 contains the details of electrode preparation (from the perspective of laboratory research), cell-assembly (three-electrode and two-electrode configuration), and the common electrochemical evaluation techniques. The thermodynamic and kinetic aspects of the various charge storage mechanism (EDLC, pseudocapacitive-combination of charge-transfer and electrosorption of ions and battery-type (intercalation-type) behaviors) of supercapacitor device are elaborated in the Section 4. It also contains the electrochemical performances (specific capacitance/capacity, cyclic stability and energy and power densities) of the various electrode materials (with the representative examples) based on their charge storage mechanism under different electrolyte and cell configuration conditions. Beyond the conventions of energy storage devices, the advanced and smart features are also integrated with the supercapacitors towards the next-generation applications (mainly, stretchable, self-healing and self-charging devices), which are discussed in the Section 5. Finally, the futuristic perspective of high-performance supercapacitors in the domains of design, fabrication, and evaluation techniques towards superior capacitance and stability are summarized in Section 6.

2. Components of Supercapacitors

2.1. Electrode Materials

The electrode materials constitute the major role among the different components of the supercapacitor device. An ideal electrode material should possess high electrical conductivity, larger electrochemically active surface area, higher electrochemical and thermal stability, and greater surface wettability. Furthermore, it must be cost-effective and recyclable. In general, several factors including morphology, porosity, and accessibility to electrolytes decide the electrochemical performances of the electrode materials. Notably, the incorporation of nanomaterials in the supercapacitors has enormously improved the device's performance. In this section, the details of extensively exploited electrode materials are concisely discussed in the following categories.

2.1.1. Carbon-Based Materials

Several carbon-based materials are known as active electrode materials for supercapacitors, including activated and mesoporous carbons [15–17]. The zero, one-, two-, and three-dimensional (0D, 1D, 2D, and 3D, respectively) carbon nanomaterials such as fullerenes, carbon nanotubes, carbon nanofibers, graphene/reduced graphene oxide, and 3D graphene derivatives are also well studied for this purpose [18]. In general, carbon-based materials have high porosity and electrical conductivity when compared to metal-based compounds as well as conducting organic polymers. For instance, activated carbon has a maximum surface area of $>3000\text{ m}^2\text{ g}^{-1}$, and a very high electrical conductivity of $\sim 10^8\text{ S m}^{-1}$ could be achieved for graphene. In addition to desirable physical properties, they have excellent chemical stability and can operate in a wide range of electrolyte systems. Among various carbon-based materials, activated carbon is broadly employed electrode material for supercapacitors, including in commercial device production. To obtain the activated carbon with high porosity and electrical conductivity, the adopted synthetic

methods are crucial and should be appropriate. To be precise, the optimum synthetic technique provides the sp^2 -hybridized carbon structure with three-dimensional morphology consisting of micro/macro pores. In a typical procedure, the carbon precursor, which could be synthetic organic molecules or derived from natural sources, is deposited over soft or hard templates (Figure 2a). The usually employed synthetic carbon precursors are phenol, resorcinol, thiourea, formaldehyde, benzoxazine, and melamine. Similarly, a variety of biomaterials derived from natural sources, namely, cellulose, starch, lignin, and chitin, are used after carbonization and activation processes [19–26]. These natural biomaterials are obtained from the abundant plant- (rice rusk, coconut shell, and seeds), coal-, and animal waste-based resources [27–29]. Porous zeolites and silicates (SiO_2) are employed as hard templates, and surfactant-based micelles as soft counterparts. The templates have inherently porous structures, which help to construct the frameworks of carbon precursors in a three-dimensional fashion. After that, the thermal pyrolysis converts the precursors into sp^2 -carbon-rich structures, and the process is called ‘carbonization’. Subsequently, the removal of the template from the above structure leads to voids from the space covered by them. The amount of porosity is further improved by treating the prepared carbonized structures with strong acidic ($H_3PO_4/ZnCl_2$) or basic (KOH/K_2CO_3) medium, known as ‘activation’. The main reason for the activation process is to create additional porosity upon itching the labile functional groups together with the sp^3 -carbon-rich domains. The activation process could also be carried out by treating the carbonized structures with a mixture of CO_2 and H_2O under higher temperatures. The latter method is considered efficient and less hazardous when compared to harsh activation conditions with acids and bases.

Fullerenes are 0D carbon nanomaterials that have cage-like structures and sizes in the range of <1 nm [30]. The fullerene with sixty carbon atoms (C_{60} , also known as Buckminsterfullerene) has fused five-membered (12 numbers) as well as six-membered (20 numbers) carbon rings, which form the nano soccer ball-like structure. Due to their excellent electron transport properties, they have extensively been in solar cell devices. Similarly, the nano/microstructures derived from fullerene-based materials are highly suitable for the fabrication of electrode materials for supercapacitors [31]. In addition, the one-dimensional carbon nanomaterial, namely carbon nanotubes, have highly conjugated hexagonal lattices of sp^2 -carbons [18]. They have a higher surface area ($1500\text{ m}^2\text{ g}^{-1}$) and excellent electrical conductivity ($\sim 10^6\text{--}10^7\text{ S m}^{-1}$), which establish them as important electrode materials for supercapacitors. In general, carbon nanotubes are synthesized via chemical vapor deposition, arc discharge method, and laser ablation process. The chemical vapor deposition technique is more suitable and widely utilized to grow vertically aligned carbon nanotube-based electrode materials. The mixture of carbon-containing gases such as CH_4 , acetylene, or ethylene and the carrier gases, namely NH_3 , N_2 , or H_2 , are used as sources for the syntheses of carbon nanotubes with the help of metal catalysts (NiO , MgO , or Alumina) at higher temperatures in the range of $700\text{ }^\circ C$. In addition to one-dimensional carbon nanotubes, their two-dimensional counterpart, namely, graphene and graphene-based materials are also employed as electrode materials for supercapacitors [32–34]. Exfoliation of bulk graphite into individual graphene layers in the solution phase is a cheap method; however, it usually provides low yields. Due to very strong intertubular/interlayer π -stacking interactions, the carbon nanomaterials exist as bundled tubular/restacked layered structures that subsequently reduce the active surface area. The covalent/noncovalent functionalization of carbon nanotube/graphene is the best option to address this issue. For example, the surface functionalization of graphene oxide, an oxidized form of graphene obtained from bulk graphite, is carried out with various inorganic/organic materials. After that, a chemical or thermal reduction in functionalized graphene oxide partially restores the hexagonal sp^2 carbon-rich π -conjugated structures that have better electrical conductivity than fully oxidized graphene oxide (Figure 2b). The above synthetic technique is proven as an efficient and scalable method to prepare a variety of graphene-based materials for supercapacitors. Apart from the 0D, 1D, and 2D carbon nanomaterials, the 3D porous ar-

chitectures (self-assembled hierarchical flower-like/crumpled sheet-like/aligned array-like structures) are also employed to develop high-performance electrode materials [35]. The 3D porous structures are usually composed of self-assembled fullerene, carbon nanotubes, or graphene derivatives [36]. In general, the controlled self-assembly (templated/non-templated) in the solution state followed by the lyophilization would lead to nano as well as microporous structures with larger surface area. The electrochemical performances of the high-performing carbon-based electrode materials are separately discussed in Section 4.

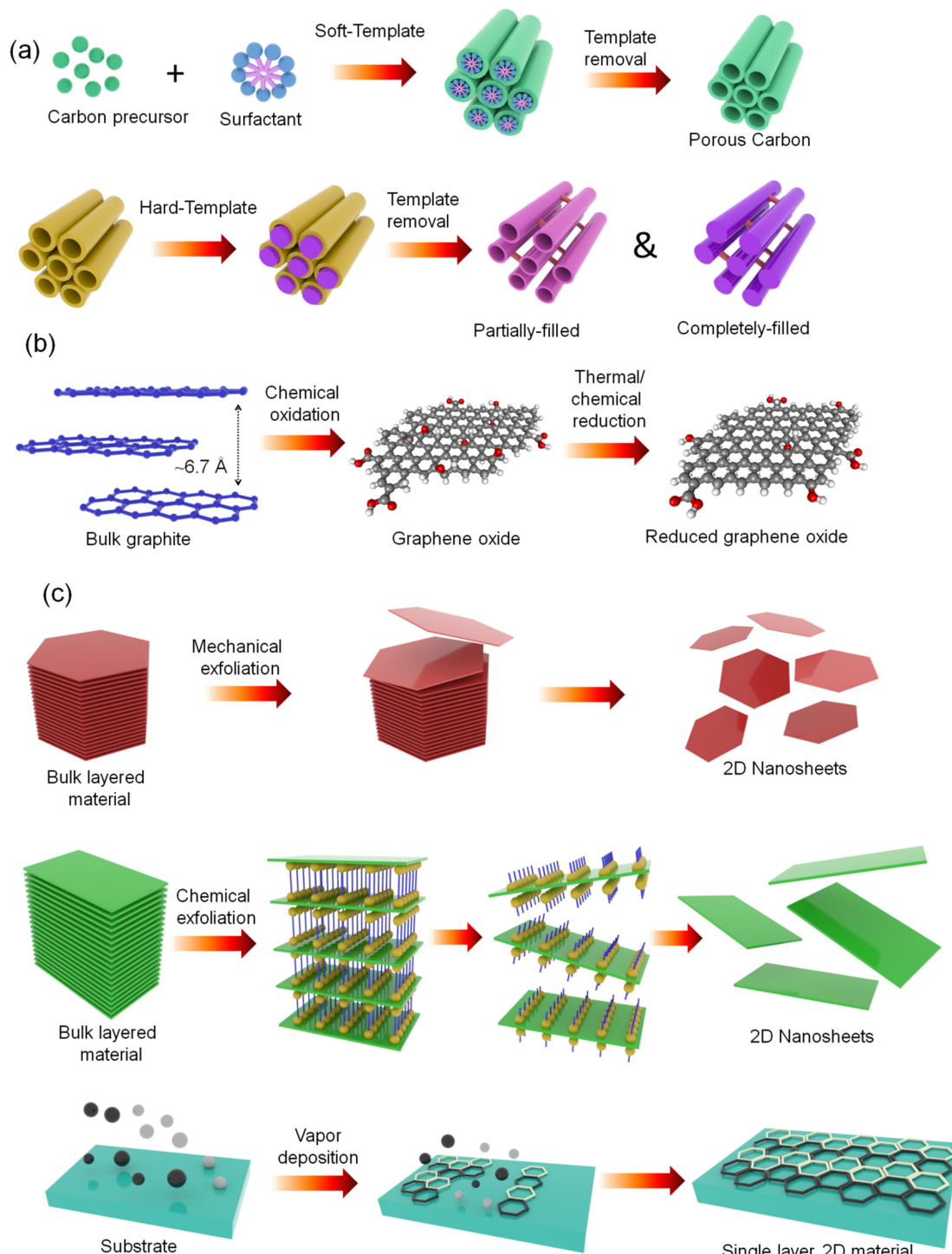


Figure 2. Various synthetic strategies of (a) activated carbon, (b) reduced graphene oxide, and (c) 2D layered materials.

2.1.2. Transition Metal-Based Compounds

A variety of transition metal-based compounds, namely, oxides, sulfides, nitrides, and phosphides, are usually employed as active materials for supercapacitors due to their reversible redox reactions, which increase the overall energy density of the device [37,38]. In particular, the transition metal oxides are preferable because of higher electrochemical stability and multiple redox states with faster charge transport of oxide lattice. For example, ruthenium oxide (RuO_2) is a well-known transition metal oxide that has been utilized extensively for supercapacitors as it has higher electrical conductivity and chemical stability [39]. However, the high cost and toxicity restrict its use towards sustainable supercapacitor devices. As cheap alternatives to RuO_2 , the oxides of vanadium (V_2O_5), manganese (MnO_2 and Mn_3O_4), cobalt (CoO and Co_3O_4), nickel (NiO and Ni_2O_3), copper (Cu_2O and CuO), and zinc (ZnO) are used as active electrode materials. The electrochemical characteristics of the transition metal oxides could further be improved by adopting binary (CoMn_2O_4 and NiCo_2O_4) and ternary (CoNiFeO_4) metal oxides, as they introduce additional redox states and enhances electrical conductivity. Furthermore, the incorporation of oxygen vacancies in the oxide lattice improves the charge storage behavior due to the increased electrode kinetics. Another counterpart of oxides, namely transition metal sulfides are also familiar electrode materials for supercapacitors. For instance, the sulfides of first-row transition metals such as manganese (MnS), cobalt (CoS , Co_3S_4 , and Co_9S_8), nickel (NiS and Ni_3S_2), and copper (CuS) demonstrate better electrochemical characteristics due to their superior structural integrity and electrode kinetics. Like transition metal oxides, the binary transition metal sulfides (NiCoS_4 , CoMnS , and CuMnS) also serve as better electrode materials than their mono-transition metal sulfides. When the oxygen and sulfur are replaced with low electronegative nitrogen, the resultant transition metal nitrides exhibit comparable electrochemical properties. Several transition metal nitrides such as VN , CrN , FeN , Co_3N , Mo_2N , and Mo_3N_2 are utilized for this purpose. Most of these transition metal compounds are synthesized by wet chemical methods from their precursor metal salts of chlorides and nitrates under hydro/solvothermal conditions. These reaction conditions provide the transition metal compounds with three-dimensionally oriented morphological features with higher porosity and electrical conductivity, which mainly determine the electrochemical performances. In addition, the charge storage characteristics of the transition metal-based compounds are further improved by preparing the composite materials with a variety of components including carbon nanomaterials and other types of transition metal compounds, which enhance electrical conductivity, porosity, and electrode kinetics [40].

2.1.3. 2D Layered Materials

The two-dimensional layered materials beyond graphene, namely, MXenes [41], layered double hydroxides (LDHs), transition metal dichalcogenides (TMDs) [42], boron nitride, and graphitic C_3N_4 have attracted interest due to their fascinating properties [43]. Among them, the MXenes [44], LDHs [45], and TMDs [46] are widely utilized as active materials towards supercapacitors. In general, the exfoliated few/monolayers of these materials have superior physical and chemical properties than their bulk structures due to the higher surface area and electrical conductivity. So, the exfoliated 2D layers are preferred to prepare the active electrode materials for supercapacitors (Figure 2c). For example, the individual layers of MXenes (M_nX_{n-1}) are extracted from a metal-ceramic phase (MAX) consisting of a transition metal (M), element (A) of IIIA/IVA group, and C/N (X). The bonding (M-X) of 'M' with 'X' is very strong because of the combined covalent, ionic, and metallic characteristics, whereas the M-A interaction is a weaker metallic bond, which makes it easier to extract the M_nX_{n-1} layers from the MAX phase. The extracted M_nX_{n-1} layers, after the removal of 'A' atoms, possess several surface vacancies and defects in the 'M' coordination positions that can accept other elements to undergo surface modifications. In general, the etching method is employed to extract the M_nX_{n-1} layers from the MAX phase with the help of hydrofluoric acid. Furthermore, the less harsh etching techniques are also utilized for this purpose by replacing the HF with a mixture of metal fluorides

(LiF and FeF₃) and HCl. In addition, the intercalation of neutral molecules (hydrazine, dimethylformamide and dimethylsulfoxide) also results in the delamination of M_nX_{n-1} layers from the bulk phase.

Another example of a 2D layered material, namely LDH, has a chemical formula of [M²⁺_{1-x} M³⁺_x (OH)₂]^{x+} [Aⁿ⁻]_{x/n} · zH₂O with bivalent (magnesium, nickel, cobalt, and zinc), trivalent (aluminum, manganese, iron, and cobalt), and anionic (chloride, nitrate, and carbonate) species [45]. The mole ratio of bivalent and trivalent metal ions varies in the range of 0.2–0.33. The basal plane of LDH is made up of M(OH)₆ units having a brucite-like structure, and it is electrostatically balanced by the counter anions to form the stacked bulk material. Most of the LDHs are synthesized by the chemical bath deposition method in the presence of divalent/trivalent metal salts and precipitating agents (ammonia or organic amines such as hexamethylenetetramine). Furthermore, electrodeposition, solvent evaporation, spin coating, and ion exchange methods are also employed to synthesize various LDH-based 2D materials. Like the MXenes, the exfoliated LDH layers show better electrochemical properties than the bulk phase. Similarly, TMDs are considered promising electrode materials for supercapacitor applications, due to their highly reversible redox processes and faster electrode kinetics [42]. The TMDs have a chemical formula of MX₂ with the transition metal (Ti, Zr, Hf, V, Nb, Ta, Mo, W, Tc, or Re) and chalcogen (S, Se, or Te). The electronic property of TMD depends on the transition metal and the chalcogen; for example, pristine MoS₂ is a semiconductor, whereas NbS₂ has a metallic character, and HfS₂ is an insulator. Similarly, the polymorphs of the same TMD show different chemical stability and electrical conductivity. The more stable 2H phase of MoS₂ is semiconducting, and its metastable 1T phase has metallic behavior. It is mainly due to the variations in the coordination types of the ‘Mo’ atom with the ‘S’ atoms. In the 2H phase, the ‘Mo’ atom has a trigonal prismatic geometry, whereas in the 1T phase, it has a distorted octahedral geometry [47]. The hydro/solvothermal methods are employed to synthesize the bulk TMDs from the precursor salts. On the other hand, the chemical vapor deposition technique is utilized to grow the individual layers over the substrate, and the chemical/electrochemical intercalation of alkali metal (Li, Na, or K) in between the layers of bulk TMDs also leads to the formation of exfoliated individual layers in solution (Figure 2c) [48]. The chemical stability and electrochemical characteristics of these exfoliated TMDs are further tuned by surface modifications.

2.1.4. Redox-Active Polymers

The redox-active polymers are better alternative electrode materials to heavy, scarce, and toxic metal-based compounds [49]. The supercapacitors with these polymers are flexible, environmentally friendly, and easily recyclable when compared to their metal counterparts. For example, redox-active polymers can easily be transformed into small organic molecules via chemical treatments, and the derived resultant molecules are used as resources for the synthesis of other organic materials. In general, redox-active polymers are classified based on their chemical structures. In certain polymers, the redox-active groups act as the backbone, and they are interconnected through the π-conjugated units [50–53]. These polymers are also categorized as ‘conducting polymers’ due to their intrinsic electrical conductivity resulting from the alternating single and double bond structure, which includes poly(*p*-phenylene), poly(*p*-phenylenevinylene), polyacetylene, polyaniline, polythiophene, polypyrrole, polyimides (perylene tetra carboxyldiimide), and poly(3,4-ethylenedioxy thiophene). They undergo reversible redox reactions upon binding/unbinding with the electrolyte ions, which impart charge storage characteristics. Some polymers have redox-active groups as pendants, mostly in a non-conjugated polymeric backbone. The commonly employed redox-active pendants are carbonyl (quinone), nitroxyl, ferrocene, triphenylamine, and organosulfur compounds. The electrochemical performances of the redox-active polymers mainly depend on the molecular weight, polydispersity, and chemical stability of oxidized/reduced species. Fine control over the molecular weight and the solution processibility is crucial to achieving high-performance

redox-active polymeric electrode materials. However, the inferior charge storage characteristics of these polymers, when compared to their metal counterparts, are overcome by compositing with the other materials having higher conductivity and redox behaviors [54].

2.1.5. Metal-Organic and Covalent Organic Frameworks

Among various inorganic and organic electrode materials, the metal-organic framework (MOF) and covalent organic framework (COF)-based materials have attracted significant interest due to their inherent porosity, electrical conductivity, and electroactive properties [55]. The MOFs are porous coordination polymers with one-dimensional to three-dimensional framework architectures created via metal coordination bonding with the organic ligands. Based on the types of metal ions and linker units, the pore size, surface area, and electrical conductivity of the resultant MOF structures are determined. The electronic properties, ionic radii, and coordination geometry of the metal ions further control the morphology and electrochemical properties. The organic linker units with different donor sites, charges, and lengths are utilized to construct the multi-dimensional framework structures. In addition, the counter ions and the nature of the solvent medium used also affect the resultant properties of the MOF architectures. Various synthetic methods are employed to prepare the MOF structures with desired properties, which include electrodeposition, chemical vapor deposition, the sol-gel method, in situ polymerization, and solvothermal/hydrothermal and co-precipitation methods. The MOF materials based on transition metals such as cobalt, nickel, iron, copper, and zinc are commonly used for supercapacitor devices. For example, the MOF structure synthesized from the cobalt ions and the fluoro-substituted terephthalic acid and hexamethylenetetramine show a layered structure with a surface area of $>12 \text{ m}^2 \text{ g}^{-1}$ and a pore diameter of $\sim 4 \text{ nm}$ [56]. When the linear linkers are replaced with a 'C3'-symmetric linker such as a triazine molecule substituted with the *p*-aminobenzoic acid groups, the higher surface area of $28 \text{ m}^2 \text{ g}^{-1}$ and the pore diameter of 44 nm are observed for the Co-based MOF structures [57]. Similarly, Ni-based two-dimensional MOF structures having the 'C3'-symmetric hexaminotriphenylene linker units are synthesized with a higher surface area of $>600 \text{ m}^2 \text{ g}^{-1}$ and the one-dimensional channel size of 1.5 nm (Figure 3a) [58]. Furthermore, the metal and heteroatoms (nitrogen and boron)-doped carbon materials derived from these MOF structures by the carbonization process at higher temperatures also demonstrate better electrochemical performance for supercapacitors [59].

Covalent organic frameworks are better alternatives to MOF-based electrode materials due to their light weight, less toxic, tunable redox activity and higher structural stability over MOFs towards the supercapacitor devices [60]. In the COF materials, the multi-dimensional porous frameworks are attained through the strong covalent bonds among the complementary linker units. For instance, the 2D COF structures comprising aminopyridine units and substituted-phloroglucinol linkers are obtained via the solvothermal method with a higher surface area of $\sim 690 \text{ m}^2 \text{ g}^{-1}$ and a pore width of $>1 \text{ nm}$ [61]. Similarly, a 2D COF structure consisting of a diaminoanthraquinone unit and the triformylphloroglucinol linker is prepared as surface-oriented thin films with a thickness of $\sim 200 \text{ nm}$. It shows the few-layered 2D nanosheets with a surface area of $>1000 \text{ m}^2 \text{ g}^{-1}$ (Figure 3b) [62]. The redox activity of these 2D COF nanosheets is further improved by incorporating a radical pendent group such as (tetramethyl piperidinyl)oxidanyl moiety (TEMPO) (Figure 3c) [63].

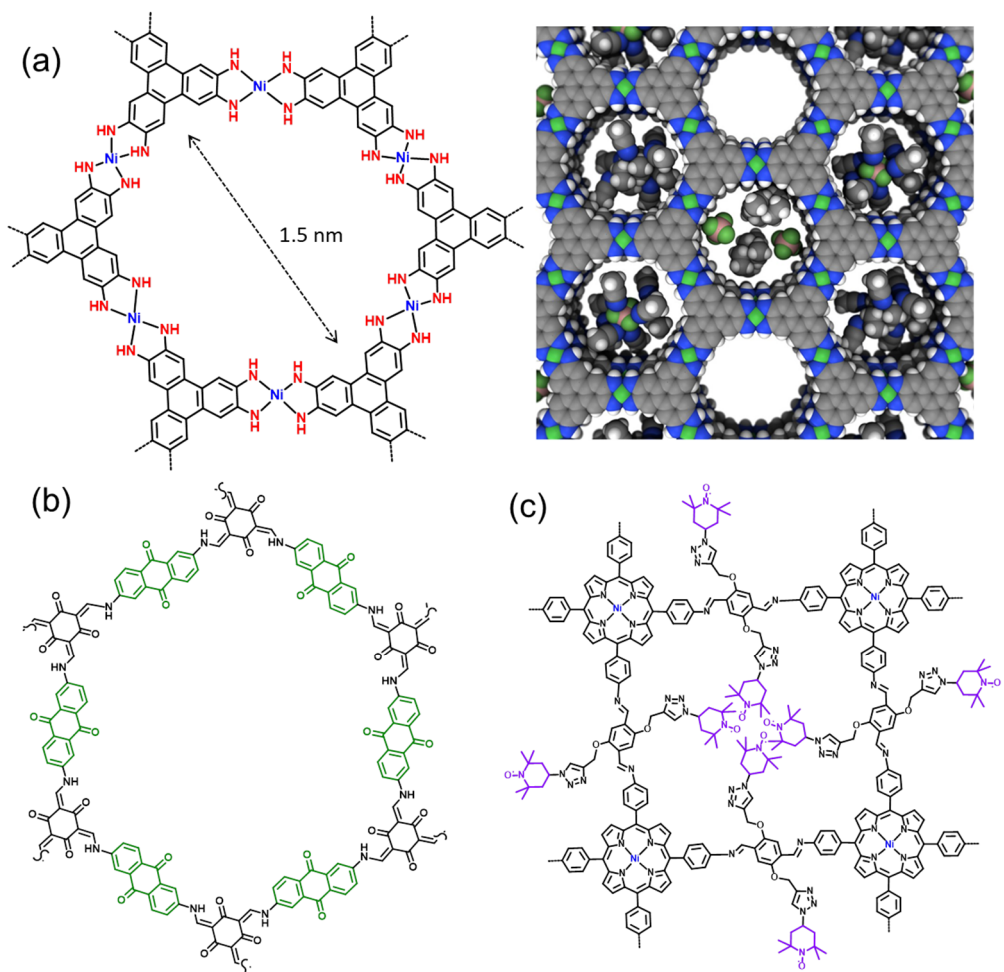


Figure 3. Chemical structure of (a) Ni-based two-dimensional MOF structures having the C_3 -symmetric hexaminotriphenylene units [58], (b) anthraquinone [62], and (c) TEMPO [63] moieties containing COF structures.

To be concise, among the various types of electrode materials discussed in this section, carbon-based materials (activated carbon, bio-derived carbon, carbon quantum dots, carbon nanotubes, and graphene derivatives) are environmentally friendly, abundant, and affordable for large-scale applications. Furthermore, they have better tunability of electrochemical performance by controlling the pore size, hydrophilicity, and conductivity via simple chemical and thermal processes. However, the lack of redox-active functionalities of native carbon materials restricts their charge storage mechanism to the electrical double-layer formation, though they often show a certain percentage of pseudocapacitance due to the oxidized carbon domains created during the material processing. To address the issue, composites based on carbon materials are frequently prepared by incorporating metal/conductive polymer-based pseudocapacitive materials. On the other hand, transition metal-based electrode materials became familiar to replace the costly and scarcer noble metal-based compounds as active electrode materials. In particular, the transition metal-based 2D layered materials are well explored as electrodes due to their intriguing properties such as tunable interlayer spacing, reactivity of induced defects (defect engineering), polymorphism and greater electrical conductivity. Furthermore, the pristine metal-organic framework (MOF) structures as well as the metal-doped interconnected carbon-based materials derived from the thermally treated MOF structures are also employed as better electrode materials due to the combined characteristics of metal domains as well as the porous carbon architectures. As the cheap and environmentally benign alternative to metal-based compounds, the redox-active polymers and covalent organic

framework (COF) structures are introduced as pseudocapacitive and battery-type electrode materials because of their intrinsic redox characteristics. Nevertheless, the electrochemical performances of the redox-active polymers and COF structures are comparatively inferior to that of metal-based electrodes. So, the development of effective synthetic protocols and unprecedented fabrication techniques would probably open up a new pathway to more sustainable as well as high-performance electrode materials.

2.2. Binder and Conductive Additives

For large-scale or commercial production of supercapacitors, the electrodes are prepared by coating or printing the slurry (a recipe consisting of active materials and additives dispersed in a solvent) of electrode materials over the suitable current collector [64]. The major additives that are employed for the preparation of electrode slurry include polymeric binders and conductive agents. The polymeric binders help the electrode material to adhere firmly over the current collector and increase the mechanical stability of the electrodes throughout the life cycle of the device. Similarly, the conductive agents are added to the electrode slurry for the enhancement of the electrical conductivity of the prepared electrodes, thereby reducing the charge transfer resistance [64]. However, the mass percentage of the additives should not be higher than 5–20% of the total mass of the slurry components. The usage of inappropriate additives partially kills the electrochemical performance of electrode materials. The commonly employed polymeric binders are poly(tetrafluoroethylene) (PTFE), poly(vinylidene fluoride) (PVDF), and poly(tetrafluorosulfonic acid)-co-(tetrafluoroethylene) (known as ‘Nafion’). The PTFE binder possesses only perfluoro ethylene units that provide hydrophobicity and insulator behavior to the electrodes, which results in poor electrolyte wettability and higher contact resistance. On the other hand, since the PVDF binder is a partially fluorinated polymer, it has higher electrochemical stability and relatively lower hydrophobicity, and is a more suitable binder additive for the electrode preparation compared to the other two polymers. The copolymer, Nafion, is a proton-conducting polymer and is used mainly for the electrode materials that show proton adsorption during the charge storage process [65]. The combination of two different polymers is also used as binder additives to improve mechanical stability and electrolyte wettability. For example, the addition of carboxymethylcellulose to the PTFE polymer considerably reduced the contact resistance and improved the adhesion of electrode materials over the current collector [66]. Poly(vinylidene chloride) and sulfonated poly(ether ether ketone) (SPEEK) polymers have also been used as binder additives for electrode preparation. The conductive additives are added to the electrode slurry to reduce the contact resistance and improve the charge transport properties of the prepared electrodes. Carbon black is a widely utilized conductive additive for electrode preparation, and is a paracrystalline carbon with a high surface-to-volume ratio [67]. It is usually prepared by the partial combustion of various carbon sources, including petroleum byproducts, coal, ethylene/acetylene gas, and so on. The carbon black obtained from the acetylene combustion is known as ‘acetylene black’ and it is also a commonly used conductive additive for supercapacitors.

2.3. Current Collectors

The current collectors play a crucial role in the preparation of electrode materials by providing physical support, especially for the powdered active materials [68]. Furthermore, they act as a medium to transfer electrons between the electrode materials and the external circuit. The total internal resistance of the fabricated supercapacitor partly accounts for the electrical resistance of the current collector as well as its interfacial resistance with the electrode materials. An ideal current collector should possess a higher mechanical strength, thermal and electrochemical stabilities, electrical conductivity, surface area, lower contact resistance, light weight, and low cost. Metal- and carbon-based materials are commonly employed as current collectors for supercapacitors. Nickel, stainless steel, titanium, copper, and aluminum are used as metal-based current collectors in the form of

foil, mesh, and foam. In general, the metal-based current collectors offer higher electrical conductivity ($\sim 6 \times 10^7 \text{ S m}^{-1}$ for Cu, $\sim 3.8 \times 10^7 \text{ S m}^{-1}$ for Al, and $\sim 1.5 \times 10^6 \text{ S m}^{-1}$ for stainless steel) and lower interfacial resistance. However, the usage of these metals as current collectors depends on the type of electrolyte systems and the operational potential window due to the corrosion and dissolution reactions [69]. For example, nickel foam is stable for alkaline aqueous electrolytes, whereas it undergoes dissolution in the acidic electrolyte. On the other hand, an alkaline medium, such as sodium and potassium hydroxide aqueous solutions, corrode the aluminum-based current collectors if they are used above the potential of 3 V [70]. Furthermore, the copper foil can only be used as a negative electrode in the potential range of 0–2 V and as a positive electrode between 3.5 and 4.5 V in the organic nonaqueous electrolyte for the lithium-ion supercapacitors [71]. In order to prevent corrosion/dissolution, the surface of the metal current collector is deposited with protective and non-reactive coatings. For example, a thin layer of carbon coating is formed over the Al/Cu/stainless steel current collector to hamper the corrosion, and it further leads to the better adhesion of electrode materials over it [72–74].

Carbon-based current collectors such as carbon cloth, carbon fiber, carbon paper, glassy carbon, and graphite foil are better alternatives to metal-based current collectors due to their high electrochemical and thermal stabilities and light weight [75]. Furthermore, they are highly preferable current collectors for large-scale and commercial device fabrications because of their great flexibility and physical strength. For example, the carbon fiber-based current collector shows better electrochemical performance than that of the carbon-coated Al current collector [76]. Furthermore, carbon paper is also used as a current collector for graphene and carbon nanotube-based electrode materials due to their flexibility and non-toxic characteristics [77]. Like metal-based current collectors, the surface modification technique is employed to improve the electrochemical performances of the carbon-based current collector. For instance, a thin layer of titanium is coated over the carbon foam to reduce the interfacial resistance with the silicon-based electrode material, which further boosts the charge storage characteristics of silicon electrodes [78]. Similarly, the doping of heteroatom, such as nitrogen-doping, is also utilized to improve the electrical conductivity and reduce the charge transfer resistance [79].

2.4. Electrolytes

As stated earlier, the major disadvantage of supercapacitor devices when compared with batteries is lower energy density, which in turn depends on capacitance and operational voltage [80]. To achieve it, high-performance electrolytes that operate in a wider potential window are required in addition to the electrode material with higher capacitance. In general, a given electrolyte can work without a considerable decomposition in a particular voltage range, which is called the ‘electrochemical stable potential window (ESW)’ [81]. The electrochemical stability of components such as salt and solvent determines the value of ESW. For the aqueous electrolytes, it usually is in the range of 1 to 1.2 V due to the water decomposition reaction at 1.23 V vs. NHE, whereas it is in the range of 2.5 to 2.7 V and 3.5 to 4.0 V for non-aqueous (organic solvents-based) and ionic liquid-based electrolytes, respectively. Furthermore, the size of ions, ionic conductivity, viscosity, and freezing point of the electrolytes also affect their performances. In this section, the various types of commonly employed aqueous, non-aqueous, and unconventional electrolytes would be covered.

2.4.1. Conventional Aqueous Electrolytes

In general, the aqueous electrolytes consist of acid ($\text{H}_2\text{SO}_4/\text{HCl}/\text{H}_3\text{PO}_4$), alkaline ($\text{KOH}/\text{NaOH}/\text{LiOH}$), or salt ($\text{Li}_2\text{SO}_4/\text{Na}_2\text{SO}_4/\text{K}_2\text{SO}_4$) solutions. The concentration of aqueous electrolyte solution is typically in the range of 0.5 to 6 M. Aqueous electrolytes have higher ionic conductivity than nonaqueous or unconventional electrolytes [82]. For instance, an aqueous solution of 1 M H_2SO_4 has a maximum ionic conductivity of $\sim 0.75\text{--}0.8 \text{ S cm}^{-2}$ at 25 °C. In order to obtain maximum ionic conductivity, the concentration of electrolyte

solution should be optimum, and a very low or very high concentration usually leads to lower ionic conductivity. Furthermore, the ionic conductivity of a given aqueous electrolyte depends on the molar ionic conductivity of hydrated cations and anions. The smallest hydronium cation shows a higher value of $350 \text{ S cm}^2 \text{ mol}^{-1}$, and the larger perchlorate anion exhibits a lower value of $67 \text{ S cm}^2 \text{ mol}^{-1}$. The charge storage capability generally increases with increasing the ionic conductivity of the electrolyte solution. For a given electrode material, it is higher in aqueous electrolytes than non-aqueous electrolytes due to the higher ion mobility and faster interfacial charge transfer kinetics.

In addition to acidic electrolytes, alkaline aqueous electrolytes are also widely used for supercapacitors because of their comparable ionic conductivity with their acidic counterparts. An aqueous electrolyte solution of KOH with a concentration of 6 M possesses a specific conductivity of 0.6 S cm^{-1} at 25°C [83]. The alkaline electrolyte is more suitable for carbon-based electrode material with a surface functional group that undergoes pH-dependent redox reactions. The transition metal (Mn, Co, and Ni) oxides, sulfides, and nitrides show better electrochemical performances in alkaline electrolytes as their redox reactions are more prominent in these conditions [84]. It further depends on the type of cation of the alkaline electrolyte; for instance, NiO exhibits higher specific capacitance in NaOH solution than in KOH due to the higher intercalating character of the former. Unlike acid and alkaline aqueous electrolytes, neutral electrolytes are extensively used for aqueous supercapacitors because of higher ESW and less corrosiveness. The chlorides, sulfates, and perchlorates of Li, Na, and K metal ions are usually employed for this purpose [85]. Among them, the aqueous solution of Na_2SO_4 is considered an effective electrolyte for transition metal oxides such as MnO_2 and V_2O_5 . For example, MnO_2 -based electrode materials show higher performance in Na_2SO_4 and NaCl electrolytes when compared to the Li and K salts. It proves that not only the size of metal ion, but also the interactions at the electrode–electrolyte interface affects the electrochemical performances of the electrode materials. Furthermore, the salts of alkaline-earth metal cation (Mg^{2+}) show higher performance for transition metal oxide-based electrodes (MnO_2) than alkaline metal salts due to the bivalency of the former, which balances more number of charges during the intercalation reaction.

Though aqueous electrolytes have many advantages, they have a few drawbacks that prevent them from extensive usage in commercial supercapacitor devices. Among them, the important disadvantage is the water decomposition reaction around the cell potential of 1.23 V vs. NHE [84]. Even though the aqueous supercapacitor devices are intended to operate below the potential window of 1.23 V, the repeated charge–discharge cycles generate hydrogen and oxygen gases at the electrodes due to the minor hydrogen and oxygen evolution reactions. The gradual accumulation of gases leads to the rupture and explosion of the device over time and it is considered a critical performance and safety issue. Furthermore, the aqueous supercapacitor cannot be operated at elevated temperatures other than atmospheric conditions because of the increased rate of water decomposition reaction at higher temperatures. In addition to that, the acid and alkaline electrolytes are highly corrosive, particularly at higher concentrations. This leads to the corrosion of electrode materials after the repeated intercalation/deintercalation processes of metal ions into the electrode materials. It further results in the peeling of active components from the surface of the current collector, which drastically reduces the charge storage capability of supercapacitors [86]. On the other hand, the neutral electrolytes, however, are less corrosive; they exhibit lower electrochemical performance when compared to the acid and alkali electrolytes due to the relatively lower ionic conductivity. In addition, the solubility of neutral salts is comparatively limited to that of acids and alkalis, which further restricts the attainment of higher concentrations resulting in lower ionic conductivity.

2.4.2. Conventional Nonaqueous Electrolytes

In the nonaqueous electrolytes, the conductive salts are dissolved in the organic solvents. In general, the salts consist of metal cations/organic ammonium ions and perchlorate/fluoride-

containing inorganic/organic anions [87]. They include LiClO₄, NaPF₆, tetraethyl tetrafluoroborate (TEA BF₄), and lithium bis(trifluoromethanesulfonyl)imide (LiTFSI). The acetonitrile or carbonate-containing organic solvents, such as ethylene carbonate (EC), propylene carbonate (PC), and dimethyl/diethyl carbonate (DMC/DEC), are used as electrolyte media (Figure 4a). The concentration of salts in the nonaqueous electrolytes varies in the range of 0.5 to 1.5 M in a single or a mixture of the above-mentioned solvents. Due to the lower solubility of these salts in the organic solvents, the ionic conductivity of the non-aqueous electrolyte is lower than that of its aqueous counterparts. However, the ESW of non-aqueous electrolytes is usually higher in the range of 2.5 to 2.8 V because of the higher electrochemical stability of organic solvents. It subsequently increases the operational potential range of supercapacitors, thereby increasing the energy and power densities. The actual ESW of nonaqueous electrolytes depends on the nature of conductive salt, organic solvent, and the amount of water contamination [81]. Conductive salts play a significant role in determining the electrochemical performances of the nonaqueous electrolyte. An ideal salt for the nonaqueous electrolyte should have higher ionic conductivity, solubility, chemical stability, and lower cost. The organic ammonium salt of TEA BF₄ is a widely used conductive salt for commercial supercapacitors. The common trend of ionic conductivities of organic ammonium cations and fluoro-/chloro-containing anions are as follows: tetramethyl ammonium ion < tetra butyl ammonium ion < tetra propyl ammonium ion < tetraethyl ammonium ion and CF₃SO₃⁻ < ClO₄⁻ < PF₄⁻ < BF₄⁻, respectively. In order to increase the solubility of conductive salts, the organic ammonium salts are asymmetrically substituted with different alkyl groups as well as cyclic aromatic groups. The triethyl methyl ammonium and 1-ethyl-1-methylpyrrolidinium tetrafluoroborate are a few examples of asymmetrical organic ammonium salts. The symmetrical and asymmetrical organic ammonium ions with bis(oxalate)borate anions also show higher solubility in organic solvents. In addition to ammonium salts, a symmetrically substituted phosphonium salt, namely, tetrakis(diethylamino)-phosphonium hexafluorophosphate exhibits better solubility and higher ESW of 3.2 V in acetonitrile solvent with the concentration of 1 M.

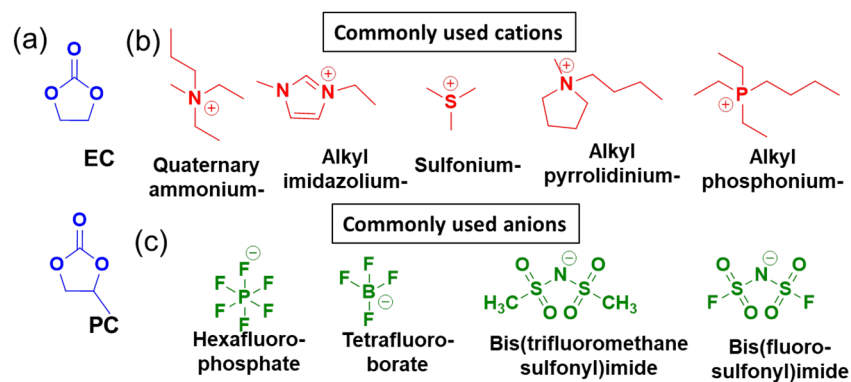


Figure 4. Chemical structures of (a) commonly used organic solvents (EC and PC), and (b) cationic and (c) anionic species of ILs.

Like conductive salts, organic solvents, too, should have better physical and chemical properties to attain high-performing nonaqueous electrolytes. A suitable organic solvent must possess high electrochemical stability, a higher boiling point, lower viscosity, and a lower freezing point. Among various organic solvents available, acetonitrile and propylene carbonate are widely utilized solvents for nonaqueous electrolytes [88]. Acetonitrile has a higher dielectric constant and lower viscosity when compared to propylene carbonate. The acetonitrile-containing nonaqueous electrolytes have better ionic conductivity than that propylene carbonate. However, the higher flash point and lower toxicity are the advantages of propylene carbonate-containing electrolytes. Both the organic solvents can be used in the operational potential window of 2.5 to 2.8 V. The other organic solvents, namely, fluoroacetonitrile, adiponitrile, propionitrile, butylene carbonate, fluoroethylene, and ethyl

isopropyl sulfone, are also utilized as they have a higher boiling point and electrochemical stability. The ionic conductivities of nonaqueous electrolytes are further increased by employing a mixture of organic solvents. The blending of two or more organic solvents in different ratios considerably lowers the viscosity as well. Mixed organic solvents such as propylene carbonate-trimethylene carbonate, ethylene carbonate-propylene carbonate, and fluoro propylene carbonate-propylene carbonate are commonly used binary organic solvents. The organic additives based on sulfites (diethyl sulfite and 1,3-propylene sulfite), esters (methyl acetate, ethyl acetate, and methyl formate), and aromatic fluorobenzenes (1,3,5-tri fluorobenzene) are often mixed with nonaqueous electrolytes to improve their electrochemical performances. In addition to higher EWS, the nonaqueous electrolytes are capable of operating in a wide temperature range of 60 to -40°C . Since the nonaqueous electrolytes could be operated even at -40°C , they are highly preferred in commercial device manufacturing, including high-end applications such as space-related devices [89].

Though nonaqueous electrolytes have several superior properties, they have a few drawbacks as well. The lower ionic conductivity is a major issue with these electrolytes. The concentration and the degree of dissociation of salts, ionic mobility, size of conductive ions, and the type of organic solvents are the crucial factors that decide the performance of nonaqueous electrolytes [90,91]. In general, the organic salts have a lower degree of dissociation in organic solvents, which in turn affects the ion mobility and ionic conductivity. The degree of dissociation of salts further decreases at a lower temperature (<10 to -30°C) in the organic solvents, and it reduces the ionic conductivity of the nonaqueous electrolytes, which are intended to work at sub-zero temperatures [92]. The electrochemically induced decomposition of organic groups at electrodes is another drawback with nonaqueous electrolytes. The salts with organic cation (TEA) or anion (TFSI) have the possibility of electrochemical decomposition over time, depending on the chemical potential of the current collector. The carbonate-containing organic solvents (EC, DMC, or DEC) also have more chance of decomposition, followed by the evolution of carbon mono/dioxide gases while going through several charging/discharging cycles [93]. In addition, the presence of impurities, such as water, considerably lowers the performance of these electrolytes. If any trace amount of water is present, it decomposes at the electrode and releases hydrogen and oxygen, as the operational potential window of nonaqueous supercapacitors is larger than that of the water decomposition potential (1.23 V). Therefore, the construction of commercial supercapacitors is usually performed under an inert atmosphere (argon or nitrogen) via a glove box set-up to avoid any moisture contaminations.

2.4.3. Unconventional Electrolytes

In liquid electrolyte systems, the molten salts (ionic liquids, ILs), superconcentrated salt solutions (water-in-salt, WIS), and deep-eutectic solvents (DES)-based electrolytes have attracted a lot of interest due to their higher operating potential window and lower freezing point, which are essential for the high energy density and superior electrochemical performances at sub-zero temperatures. The ionic liquids are molten salts comprising organic cations and organic/inorganic anions with melting points below 100°C [94]. They have high chemical and thermal stabilities, very low volatility, and non-flammability. Furthermore, based on the type of cations and anions, the properties of the ionic liquids can be tuned easily. The typical cations include ammonium, imidazolium, sulfonium, pyrrolidinium, and phosphonium ions (Figure 4b), and the hexafluorophosphate, tetrafluoroborate, bis(trifluoromethane sulfonyl)imide and bis(fluorosulfonyl)imide are the commonly used anions for the ILs (Figure 4c) [95]. When compared to the conventional organic electrolytes, the ILs have a higher electrochemical stability window, more than 3 V, due to higher resistance towards the decomposition. However, ILs possess many downsides, namely low ionic conductivity and high viscosity. For example, the 1-ethyl-3-methylimidazolium (EMIM)-based ILs show a higher ionic conductivity of $\sim 14\text{ mS cm}^{-1}$ among the other ILs, which is four-fold lower than that of an organic electrolyte at 25°C (TEABF₄ in acetonitrile) [96]. Similarly, the EMIM BF₄ has a viscosity of 41 centipoise, which is very high

when compared to the acetonitrile-based electrolytes (0.3 centipoises). The higher viscosity and lower ionic conductivity eventually increase the charge transfer resistance that subsequently reduces the rate performance of the supercapacitor. However, the proper chemical design can overcome these limitations to a considerable extent. For example, a tetracyanoborate (TCB)-based IL, such as EMIM TCB, shows a relatively higher ionic conductivity and low viscosity of 1.3×10^{-2} S cm⁻¹ and 22 cp, respectively [97]. In addition, the other widely used cations and anions for ILs are categorized as N-substituted azepanium-, propylpiperidinium- and 1-methoxymethyl-1-methylpyrrolidium- for the former and the dicyanamide, bis(fluoro sulfonyl)imide, and tris(pentafluoroethyl) trifluorophosphate for the latter.

The WIS-based electrolytes are preferable among the various unconventional electrolytes due to their higher electrochemically stable potential window, environmental friendliness, and flame retardancy [98]. In general, the WIS electrolytes are highly concentrated salt solutions with the usual concentration range of 17 molal (m) to 33 m. The commonly used salts for the WIS electrolytes are LiTFSI (21 m), ZnCl₂ (30 m), LiNO₃ (22 m), NaClO₄ (17 m), NaNO₃ (12 m), and ammonium acetate (30 m) [99]. The WIS electrolyte with a mixture of two or more salts is also developed to obtain high-performance electrolytes. In particular, the ESW range of WIS electrolytes, which depends on the number of free water molecules, is increased by the mixture of salts containing common cations or anions [100]. The additional cations or anions coordinate with the free water molecules that constantly decompose on the electrode surface when the operating potential window crosses the water decomposition voltage (1.23 V vs. NHE), and it subsequently increases the ESW (Figure 5a). For example, the ESW of 21 m LiTFSI electrolyte (<3 V) is increased beyond 3.1 V upon the addition of lithium triflate (7 m) (Figure 5b) [101]. Similarly, the mixed WIS electrolyte consisting of tetraethyl triflate (22 m) and sodium triflate (9 m) salts exhibits a wider ESW of 3.3 V that is eventually higher than that of individual salt solutions (Figure 5c) [102].

DES-based electrolytes are another alternative with higher ESW, low volatility, and non-flammability towards high-performance supercapacitor devices [103]. The DES is generally a mixture of two components with a certain mole ratio, and furthermore, it exists in a liquid phase due to a lower melting point than that of its individual components. The stronger intermolecular interactions such as hydrogen bonding, Lewis acid–Lewis base interactions, and van der Waals forces among the cation/anion and the functional groups of the organic component lead to the complex amorphous network-like structures that effectively prevent the solidification of solids [104]. In particular, the DES electrolytes achieved from the mixture of salt (metal chloride, perchlorate, sulfonamide, and ammonium/quaternary salts) and a small organic molecule with functional groups such as -OH, -C=O or -N-H are majorly stabilized with very strong hydrogen bonding interactions (~ 4 kJ mol⁻¹). Similarly, the mixture of electron-deficient molecules (BF₃ or AlCl₃; Lewis acid) with another molecule-having electron-donating functional group (-O-, -C=O, -O-CO-O- or -N-H; Lewis base) also forms DES electrolyte, due to the Lewis acid–Lewis base interactions (~ 4 to >100 kJ mol⁻¹). Though the interaction energy of van der Waals forces is relatively weak (0.4 to <4 kJ mol⁻¹), they also rarely participate in the formation of DES electrolytes. The common salts employed for DES electrolytes are LiTFSI, LiClO₄, lithium difluoro(oxalato)borate, zinc perchlorate, and the functional molecules as urea, acetamide, N-substituted acetamide, thiourea, choline chloride, and so on. Like ionic liquids, DES electrolytes suffer lower ionic conductivity and higher viscosity. The DES electrolyte of LiTFSI: N-methyl acetamide shows an ionic conductivity of 1.35 ms cm⁻¹ and a viscosity of 78 mPa.s at 25 °C, though the ESW is high, at 4.7–5.3 V [105]. Furthermore, the physicochemical properties of DES electrolytes are improved by adding a fraction of water, or other organic solvents (acetonitrile or propylene carbonate) that decrease the viscosity and improve the conductivity through the ESW are slightly traded-off (Figure 5d). The addition of 30% of water to the dual-salt DES electrolyte of urea, LiTFSI, and Zn(TFSI)₂ improves

the conductivity to 1.85 ms cm^{-1} from the lower value of 0.084 ms cm^{-1} , and subsequently leads to the lower viscosity of $0.139 \text{ Pa}\cdot\text{s}$ (Figure 5e) [106].

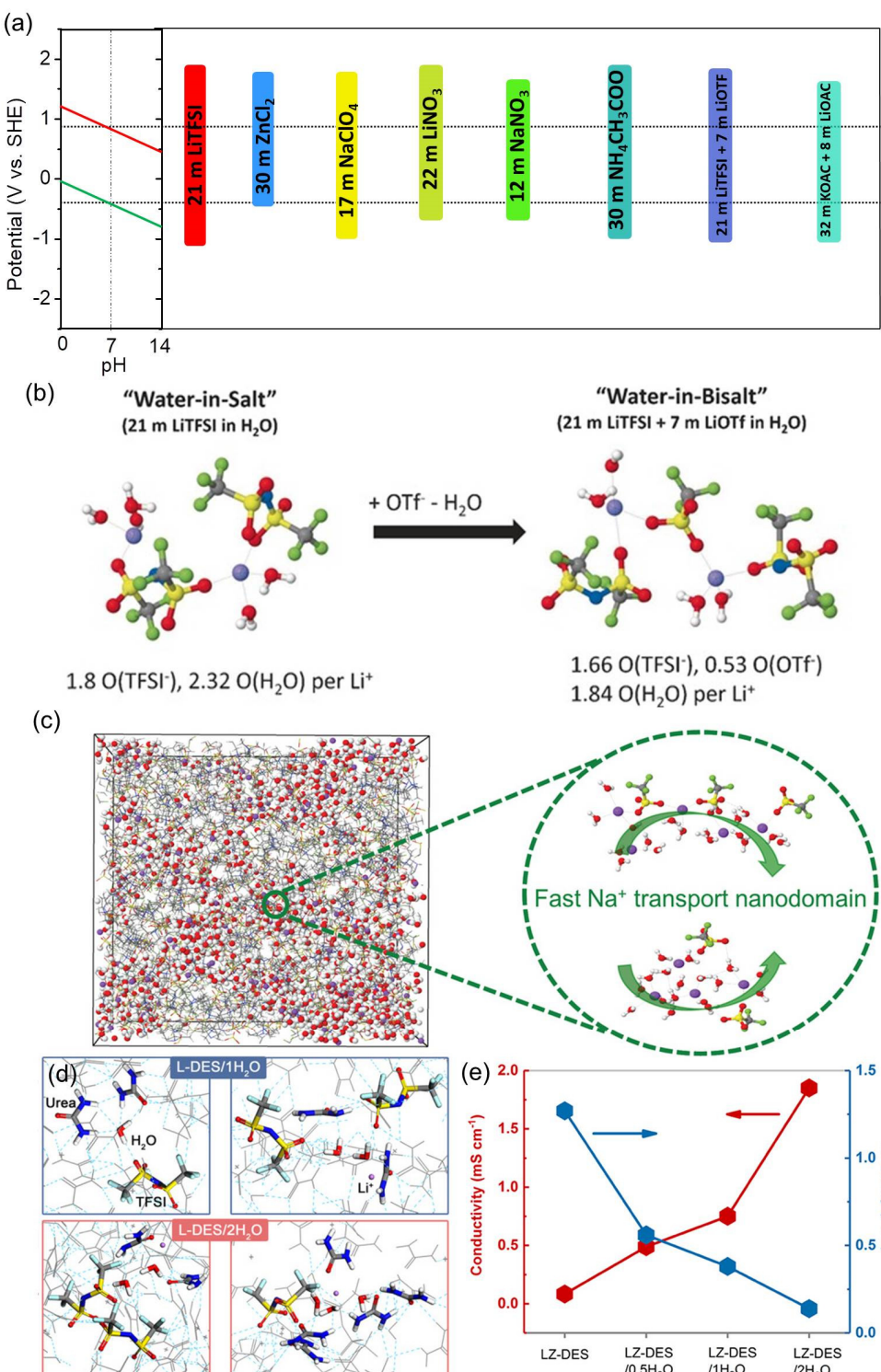


Figure 5. (a) Plot showing the ESW of various WIS electrolyte systems. Schematic representations indicating the intermolecular interactions of (b) LiTFSI/LiOTf [101] and (c) NaOTf/TEAOTf-based WIS electrolytes [102]. (d) Diagrams of equilibrated Li-based DES electrolyte, and (e) plot of ionic conductivity and viscosity changes in Li/Zn DES electrolyte upon addition of various amounts of water [106].

2.5. Separators

In addition to electrode and electrolyte materials, separators [107] with higher physical strength, ion permeability, and thermal and chemical stabilities are crucial for high-performance supercapacitors [108]. In the two-electrode cell and commercial supercapacitors, the separator plays a significant role in preventing any short circuit by the physical contact of positive and negative electrodes throughout the lifecycle of the device and, at the same time, it allows the free flow of ions across it [109]. Any damage to the separator component leads to the catastrophic collapse of the supercapacitor performance. A typical membrane separator should possess a low thickness, high dielectric constant, electrochemical stability, ionic mobility, macroporosity, and electrolyte wettability. Several varieties of separators are commonly used for supercapacitors that include polymer membrane-based separators, paper-based separators, and inorganic/ceramic separators. Synthetic techniques such as electro-spinning, phase inversion, and 3D printing methods are generally utilized approaches for the preparation of separators [110]. The polymer membrane-based separators are highly preferable for supercapacitors due to their low cost and higher physical and chemical stabilities. Polypropylene (commercially known as ‘Celgard’, a widely used separator for supercapacitors), poly(vinylidene fluoride), poly(vinyl chloride), and poly(ethylene oxide) are a few examples of polymer-based membrane separators. Based on the type of electrolyte systems (aqueous/nonaqueous), the selection of membrane separator varies; for example, the poly(vinylidene fluoride) or a copolymer of vinylidene fluoride and hexafluoropropylene is used for the organic electrolytes. However, the polymer-based separators suffer from a lower dielectric constant, which is crucial for attaining higher power and energy densities. Incorporation of ceramic materials, which inherently have a higher dielectric constant and ionic conductivity, improves the electrochemical performances of the polymer-based separators. For example, a ceramic material such as titanium dioxide is added to the poly(vinylalcohol) to improve the ionic conductivity, porosity and mechanical strength [111]. Similarly, the poly(vinyl butyral) with 1D aluminum oxide nanorod exhibits high porosity, high strength of >30 MPa, thermal stability up to 200 °C, electrolyte uptake of >200 wt% without swelling, and ionic conductivity of ~14 mS cm⁻¹ [112]. In addition to synthetic polymers, the biopolymer [113] (cellulose and its derivatives) and bio-membranes such as egg-shell-based materials [114] are also employed as separators for the supercapacitors. The paper-based separators derived from natural cellulose resources are highly preferred for large-scale fabrications, even with organic solvents, due to high porosity and mechanical stability [115,116].

3. Electrochemical Characterization of Materials (Electrodes and Electrolyte Systems) and Assembly-Testing of Supercapacitors

The electrochemical performances of the electrode materials and electrolytes, which are the two key components of the supercapacitor, are tested by using a three-electrode cell before making the actual two-electrode devices. For laboratory testing purposes, the electrode material of interest is converted into a ‘working electrode’. Based on the physical state of the electrode materials, the process of preparation of the working electrode is varied. In most cases, the electrode materials are powdered samples, except free-standing and in situ-grown active materials [117]. Therefore, the powdered electrode materials should evenly be coated over a conductive substrate, which may be a metal foil/foam or conductive carbon fabric, to prepare the working electrodes. In order to make a uniform coating of electrode materials, the slurry formulation is made with a few additives, such as a polymer binder and conductive carbon in an organic solvent at a weight percentage of 5–20% with respect to the electrode material. These additives are used to improve the stability and electrical conductivity of the coating over the current collector. The homogenized slurry is coated on the current collector by various methods, such as spray and dip coating, the doctor blade method, and drop casting. In general, for laboratory testing, the area of the working electrode may vary from 1 to a few cm², and the mass density may be in the range of several mg cm⁻² to a few tens of mg cm⁻². The prepared working electrode

is now connected to an auxiliary electrode and a reference electrode in a three-electrode configuration. The purpose of auxiliary and reference electrodes is to close the electrical circuit and to control the applied potential (potentiostatic) or passing current (galvanostatic) of the working electrode during the measurement, respectively. A few reference electrodes, namely, silver–silver chloride, calomel, or Hg/HgO electrodes are used based on the electrolyte systems. In general, a compartmentalized platinum foil with a large area is conventionally used as an auxiliary electrode. The use of platinum sometimes contaminates the electrode and electrolyte solution, due to the subsequent oxidation as well as reduction reaction at the surface of the auxiliary electrode depending upon the working electrode reaction. To avoid contamination, a graphite rod is employed as an auxiliary electrode. In order to investigate the electrochemical performances of a given electrode material for a supercapacitor device, certain parameters, such as specific capacitance, energy, and power densities, are calculated with the help of various electrochemical techniques. These methods are versatile and dynamic techniques that assess the electrochemical characteristics of the electrode materials by monitoring the potential and current changes. The detailed analyses of the plots obtained from the measurements provide information on the mechanism and electrode kinetics. Among various electrochemical techniques, cyclic voltammetry (CV), galvanostatic charge–discharge (GCD), electrochemical impedance (EIS), and linear-sweep voltammetric (LSV) measurements evaluate most of the electrochemical characteristics of the electrode as well as electrolyte materials [118]. The main purpose of electrochemical characterization of electrode and electrolyte materials in the three-electrode configuration is to identify the reversibility of the individual electrode processes, the stable operational potential window, and the charge-transfer kinetics at electrode–electrolyte interfaces. After successful electrochemical characterizations, the actual supercapacitor device is fabricated in a two-electrode configuration for laboratory testing. In the two-electrode configuration, the device has a positive electrode and a negative electrode. A separator soaked with the electrolyte solution is sandwiched between the electrodes to complete the two-electrode cell. For a given electrode material, it can act as either a positive or negative electrode depending upon the material property, which is identified with the help of the CV experiment. The charge–discharge behavior, cyclic stability, and device resistance are investigated by using the above-mentioned techniques for the two-electrode cell. The various electrochemical techniques are briefly discussed in the following sub-sections.

3.1. Cyclic Voltammetry

In a typical CV technique, the current response of electrode material (working electrode) is measured when a potential is applied with the help of a reference electrode [119]. The CV measured by monitoring the current response during the two linear potential sweeps in a cyclic manner is called a cyclic voltammogram. At first, the potential is swept at a rate ($V\ s^{-1}$) from an initial voltage ' V_1 ' to a final voltage ' V_2 ' in the first linear potential sweep, and subsequently, it is reversed back to ' V_2 ' from ' V_1 ' in the second potential sweep. In general, the CV is rectangular or quasi-rectangular in nature (Figure 6a,b). From the shape of the obtained CV, the mechanism of charge storage (electrical double-layer capacitance or pseudocapacitance) is predicted. Mathematically, the current response ($I(t)$) is related to the capacitance (C) and the potential sweep at a particular rate ($\frac{dV(t)}{dt}$) as given below:

$$I(t) = C \frac{dV(t)}{dt} \quad (1)$$

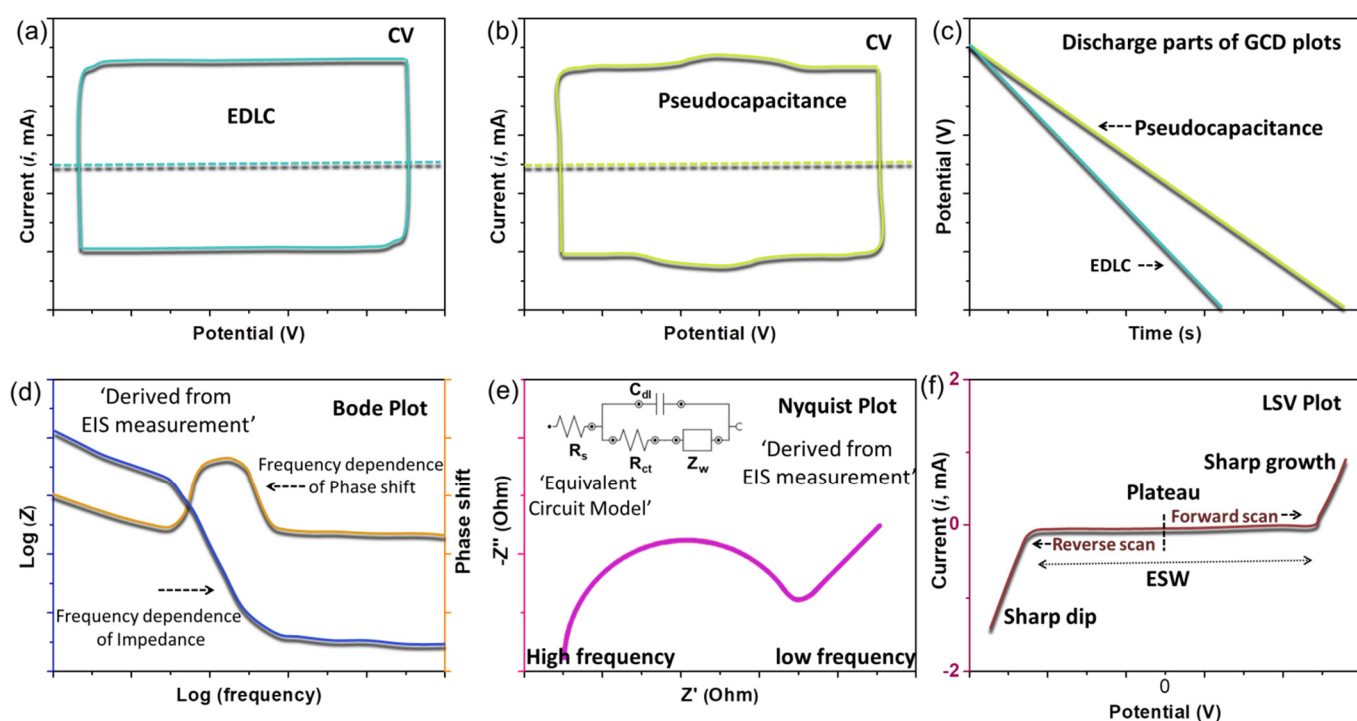


Figure 6. Typical (a,b) cyclic voltammograms, (c) discharge part of a galvanostatic charge-discharge (GCD), (d) Bode, (e) Nyquist plots, and (f) linear-sweep voltammogram.

From the cyclic voltammogram, the specific capacitance (C_{sp} , F g^{-1}) of the electrode material can be calculated by modifying Equation (1). When a cyclic voltammogram is measured in a three-electrode configuration for an electrode material with a mass ' m ' (g) at a scan rate of ' v ' (V s^{-1}) in a voltage range of ' ΔV ', the ' C_{sp} ' is described as shown in Equation (2) by assuming that the capacitance contribution from the auxiliary electrode is made much larger than the working electrode by the potentiostat ($\frac{1}{C_{cell-3E}} = \frac{1}{C_{working}} + \frac{1}{C_{auxiliary}} = \frac{1}{C_{working}}$; when $C_{working} \ll C_{auxiliary}$ (Approximation 1)).

$$C_{sp} = \frac{\int_{V1}^{V2} IdV}{m \times v \times \Delta V} \quad (2)$$

where ' $\int_{V1}^{V2} IdV$ ' is calculated by integrating the area under the CV. It should be noted that the above equation is valid only for the capacitance calculation if the CV is rectangular or very close to a rectangular shape. Furthermore, the specific energy (Wh kg^{-1}) and specific power (W kg^{-1}) of the electrode material can also be calculated from the following Equations (3) and (4).

$$E = \Delta V \frac{\int_{V1}^{V2} IdV}{3600 \times m \times v} \quad (3)$$

$$P = \Delta V \frac{\int_{V1}^{V2} IdV}{m} \quad (4)$$

3.2. Galvanostatic Charge–Discharge (GCD)

In a GCD technique [120], a constant current is applied to the electrode material, and the voltage variations are measured in a given potential range (' V_1 ' to ' V_2 ' for a positive constant current and vice versa for a negative constant current) as a function of time, which is technically termed 'current reversal chronopotentiometry'. When a positive constant current is applied to the working electrode, the potential growth is measured from an initial voltage ' V_1 ' to a final voltage ' V_2 ' against time (t , s), and then subsequently, a negative

constant current with the same magnitude is applied to the electrode to follow the potential step-down. Like cyclic voltammograms, the shape of GCD profiles also varies based on the charge storage mechanism and kinetics. For an ideal capacitor, the shape of the galvanostatic charging profile is linear (triangular shape for a complete charge–discharge cycle) (Figure 6c). It is considered the most reliable technique to calculate the specific capacitance (the amount of charge (Q) stored per unit mass (g) of material in a given potential window (V), C_{sp} ; Equation (5)), energy (E, Wh kg⁻¹; Equation (6)), and specific power (P, W kg⁻¹; Equation (7)) values of a given electrode material. Furthermore, the other crucial electrochemical behaviors such as the rate capability (variations of capacitance at different magnitudes of constant current), the cyclic stability (variations of capacitance at different numbers of repeated GCD cycles), and the columbic efficiency (ratio of the charge stored and delivered by the electrode material at the positive and negative constant currents) are also evaluated by the GCD technique.

$$C_{sp} = \frac{i \times t}{m \times \Delta V} \quad (5)$$

$$E = \frac{1}{2} C_{sp} V^2 \quad (6)$$

$$P = \frac{E}{t} \quad (7)$$

where ' i ' is the magnitude of constant current (A), ' t ' is the time interval (s) to reach the final voltage ' V_2 ' from the initial voltage ' V_1 ' and vice versa (also called charging and discharging time, respectively), ' m ' is a mass of the electrode material (g), and ' ΔV ' is the potential difference between the initial ' V_1 ' and final voltage ' V_2 ' values.

3.3. Electrochemical Impedance Spectroscopy (EIS)

In general, the EIS is a measure of impedance (i.e., the opposition of an electrical circuit to the passing current) as a function of frequency in the presence of low-amplitude alternating potential superimposed over a steady-state voltage [121]. The EIS data are represented as a ‘Bode’ plot as well as a ‘Nyquist’ plot. For example, in a ‘Bode’ plot, the average impedance/phase shift is traced against the frequency (Figure 6d). Furthermore, the frequency dependence of the system could clearly be obtained from it. In the case of the Nyquist plot, the real part of the impedance (Z') is plotted as a function of imaginary impedance (Z'') at different frequencies (Figure 6e). From the Nyquist plot, the two important parameters such as solution resistance ' R_s ' and charge-transfer resistance ' R_{ct} ', are evaluated. These values are depicted from the semicircle formed at the real part of the impedance in the high-frequency region with an angle of 45° or 90°. In addition, the fitting of the Nyquist plot with the ‘Randles’ circuit model (inset of Figure 6e) provides the other significant parameters, such as capacitance contributed from the double-layer formation ' C_{dl} ' and Warburg impedance (Z_w). The slope of the Warburg line at the lower frequency region also elucidates the charge storage mechanism of the electrode materials. Furthermore, the ' C_{dl} ' could be correlated with the frequency (f) and the imaginary impedance (Z''), as shown in Equation (8) (this equation is valid only for a simple series-RC circuit model) [122].

$$C_{dl} = -\frac{1}{Z'' \cdot 2\pi \cdot f} \quad (8)$$

3.4. Linear-Sweep Voltammetry (LSV)

The LSV technique is mainly used to evaluate the electrochemically stable potential window (ESW) of the electrode as well as electrolyte materials [123]. In an LSV method, the potential is increased linearly at a constant scan rate, and the current response is plotted against the applied potential. The current response is measured as two separate measurements, such as a forward scan (zero to positive potential region) and a reverse

scan (zero to negative potential region). A typical LSV can be divided into two regions where the current response follows a plateau and a sharp growth/dip at higher/lower potential values, respectively (Figure 6f). The plateau at a particular potential range indicates the formation of a double-layer formation that is proportional to the charge-storing capability and the potential scan rate. The sharp increase/decrease in current response at higher/lower potential regions reveals the occurrence of irreversible Faradaic processes, such as the decomposition of the electrolyte. The above potential plateau also exhibits the range of voltage window where the electrolyte can be operated without considerable decomposition (ESW).

4. Charge Storage Mechanism and Electrochemical Kinetics of Electrode–Electrolyte Interfaces

Understanding the electrode–electrolyte interface that constitutes the crucial regions where the various electrochemical processes occur is a significant step to achieving a high-performance energy storage device [124]. When an electrode that is already in contact with the electrolyte medium is applied with potential (potentiostatic) or current (galvanostatic), three kinds of processes could occur at the electrode–electrolyte interface. In one kind, the charges (electrons) are transferred across the interface due to the oxidation or reduction reaction. Depending upon the amount of reaction that takes place, the current flows through the external circuit, which is called the ‘Faradaic process’ as it follows the electrochemical laws of M. Faraday. The electric energy stored by the Faradaic process is termed ‘Pseudocapacitance’. In another type, the charge transfer is thermodynamically or kinetically least-favorable across the interface, and it is termed a ‘non-Faradaic process’. However, adsorption or desorption of electrolyte ions can occur, and it is also called the formation of an ‘electrical double layer (EDL)’. The charge stored by the EDL is known as ‘electrical double-layer capacitance’ (EDLC). Though no electron transfer happens at the interface, the current would flow in the external circuit that depends on the electrode material, electrolyte system, and the applied potential. In some cases, the diffusion of electrolyte ions into the electrode material could occur if the porosity of the electrode and the size of the electrolyte ions are appropriate. The above characteristic is called ‘battery-like’ behavior. For a given electrode material, any one of these three processes or the combination of them at different magnitudes may occur. Furthermore, the extent of individual processes highly depends on the type of electrode as well as electrolyte materials.

4.1. Charge Storage Mechanism Based on the Electrical Double-Layer Formation

For the electrode materials that have a non-faradaic process, the electrode–electrolyte interface behaves similarly to that of a conventional capacitor [125]. If an electrode is applied with a given potential, let us consider the charge accumulated on the electrode as ‘ Q_{ed} ’ and for the electrolyte as ‘ Q_{et} ’ in the vicinity. At all times, $Q_{ed} = -Q_{et}$; here, the minus sign indicates the accumulation of an opposite charge on the electrolyte side with respect to the electrode surface. The ‘ Q_{ed} ’ symbolizes the presence of excess or deficient electrons that occupy the very top of the electrode surface with approx. the thickness of $<0.1 \text{ \AA}$ at the interface region. The excess cations or anions of the electrolyte in the vicinity of the interface constitute the ‘ Q_{et} ’. The whole arrangement of charges (cations and anions) and the solvent dipoles at the electrode–electrolyte interface is collectively called an ‘electrical double layer’. The electrolyte side of the EDL is made of several layers of reorganized solvent dipoles and solvated ions. The very first layer of solvent dipoles adsorbed on the electrode surface is called ‘inner Helmholtz or Stern layer’ and then the next adsorbed layer of solvated ions over the inner layer is known as ‘outer Helmholtz layer’. The interaction between the electrode surface and the solvent dipoles and solvated ions is purely electrostatic in nature. Beyond the outer Helmholtz layer, the free solvent molecules and the solvated ions are randomly distributed from the outer layer to the bulk medium, which is called the ‘diffuse layer’. The thickness of the diffuse layer is usually in the range of $\sim 100 \text{ \AA}$ for the electrolyte solution with a concentration of 10 millimolar.

The EDL at the electrode–electrolyte interface can be represented by a simple resistor–capacitor (RC) circuit model (based on the ‘approximation 1’ of Section 3.1.) as given in the inset of Figure 7a. When a potential (V) is applied to the electrode, the respective voltage values at the resistor (R) and the capacitor (C) are ' V_R ' and ' V_C ' and it is mathematically depicted as Equation (9). Furthermore, based on the relationship of charge (Q) on a capacitor with the applied potential (Equation (10)), Equation (9) can be modified to Equation (11).

$$V = V_R + V_C \quad (9)$$

$$Q = C_{EDL} V_C \quad (10)$$

$$V = V_R + V_C = iR_s + \frac{Q}{C_{EDL}} \quad (11)$$

where ' i ' is current (A) and ' R_s ' is the resistance of the electrolyte solution. When the applied potential of the RC circuit is varied at a given rate (v , $V\ s^{-1}$), the resultant potential and current traces against the time (t , s) are shown in Figure 7a,b. At this condition, Equation (11) can be modified to Equations (12) and (13) by considering the relations of ' $V = vt'$ and ' $i = \frac{dQ}{dt}$ '.

$$vt = R_s \frac{dQ}{dt} + \frac{Q}{C_{EDL}} \quad (12)$$

$$i = vC_{EDL} \left(1 - e^{-\frac{t}{R_s C_{EDL}}}\right) \quad (13)$$

When the potential sweep starts, the current increases and reaches a constant value of ' vC_{EDL} ', and it is subsequently used to calculate the ' C_{EDL} ' if the time is constant, and ' $R_s C_{EDL} \ll v$ '. Interestingly, if a triangular wave is applied to the RC circuit (Figure 7c), the steady-state current values are equal to ' vC_{EDL} ' and ' $-vC_{EDL}$ ' for the forward and reverse scans, respectively (Figure 7d,e). In a typical CV measurement, a triangular potential wave is applied to the electrode at a particular scan rate. If the current response is plotted against the applied potential, the shape of the cyclic voltammogram is rectangular for an ideal EDL-based material. Similarly, if a constant current (positive and negative) is passed through the electrode in a galvanostatic charge–discharge (GCD) measure, the traces of potential response against the time (GCD curve) adopt a triangular shape. Practically, from the CV and GCD measurements, the shape of plots predicts the mechanism of charge storage operated in a given electrode material.

In general, the carbon-based materials show the EDLC behavior towards the supercapacitor devices in mostly conventional aqueous electrolytes [126]. In this section, the electrochemical properties of the high-performing carbon-based electrode materials, including their composites, are summarized with a few representative examples. The mesoporous carbon doped with nitrogen atom is prepared from the benzoxazine precursor via a hard-template method utilizing the silica sieves (SBA-15) followed by the carbonization at 800 °C (Figure 8a) [127]. When the N-doped mesoporous carbon is tested in a three-electrode configuration, it shows the highest specific capacitance of ~428 F g⁻¹ at 250 mA g⁻¹. In a two-electrode device, it exhibits capacity retention of >98% even after 20,000 cycles at 5 A g⁻¹ and possesses the maximum energy and power densities of 11 Wh kg⁻¹ and ~250 W kg⁻¹, respectively. A porous activated carbon was obtained from the biopolymer (Chitin) via polystyrene templating and the carbonization at 220 °C, followed by the KOH activation process [128]. The porosity of the resulting activated carbon is tuned by changing the loading amount of polystyrene latex in the synthetic step. It has a higher specific capacitance of 567 F g⁻¹ at 500 mA g⁻¹ and capacity retention of 73% after the GCD test of 10,000 cycles (Figure 8b). The preparation of composite material with the reduced graphene oxide improved the electrochemical performances of the pristine activated carbon due to the enhanced electrical conductivity and porosity [129]. The graphene composite mate-

rial with a density of 1.23 g cm^{-3} is achieved by the thermal treatment of straw-based biomass and graphene oxide precursors. The higher volumetric capacitance of 775 F cm^{-3} at 500 mA g^{-1} is observed for the graphene composite under the three-electrode configuration. The supercapacitor fabricated from the composite material possesses better flexibility and stable performance (Figure 8c). It also delivers the higher energy and power densities (10 W h L^{-1} and $\sim 61 \text{ WL}^{-1}$) and the capacitance retention of $>93\%$ after 10,000 cycles (Figure 8d). Similarly, an ionic liquid-based non-conventional electrolyte is also employed to test the EDLC behavior of the carbon-based electrode material. For example, an ionic liquid composed of 1-butyl-3-methylimidazolium tetrafluoroborate (EMIMBF₄) and triethyl phosphate is tested with the porous carbon material in a symmetrical two-electrode configuration [130]. The device exhibits a specific capacitance of 53 F g^{-1} at 500 mA g^{-1} and the energy and power densities of 43 Wh kg^{-1} and $\sim 12 \text{ kW kg}^{-1}$. Due to the non-freezing nature of the ionic liquid electrolyte, the device can be operated even at -20°C with $>53\%$ of its initial specific capacitance. The electrochemical performances of a few representative examples of carbon-based EDLC materials are compared in Table 1.

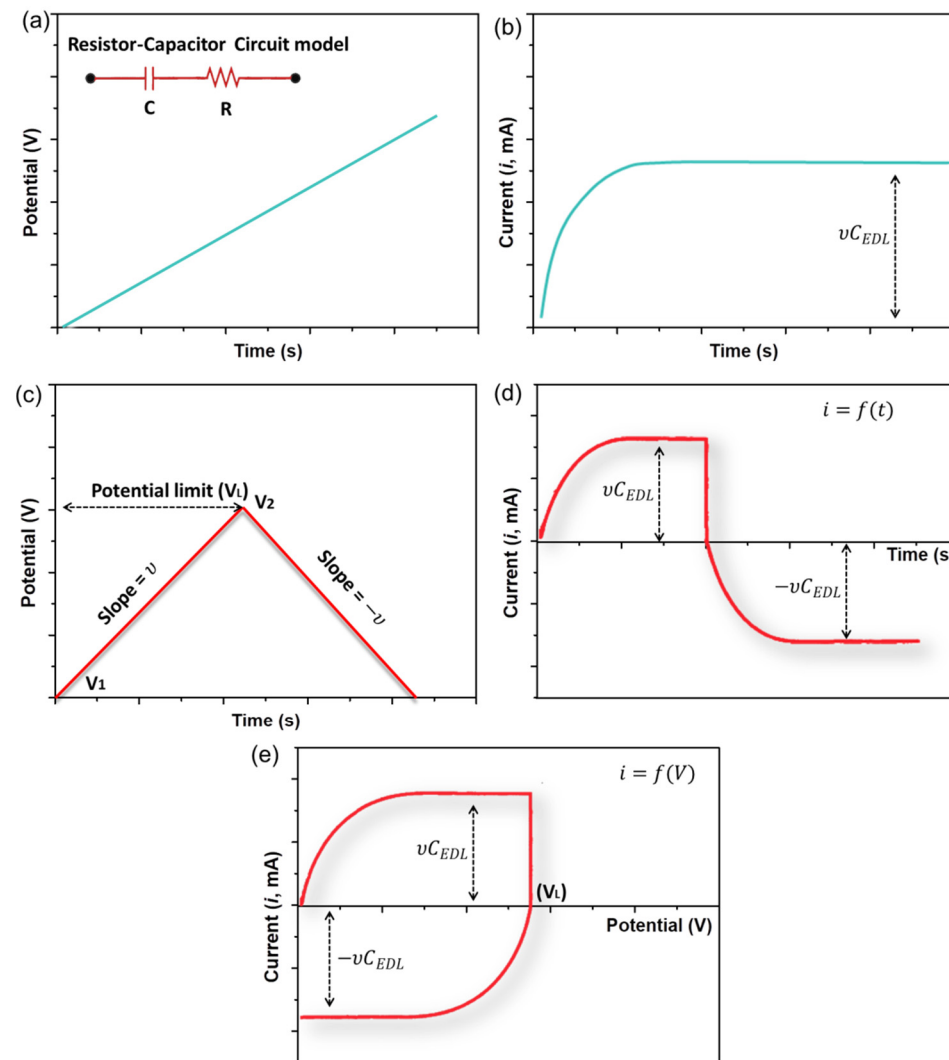


Figure 7. Plots of (a) a linear potential sweep (inset shows the pictorial representation of a simple resistor–capacitor (RC) circuit model) and (b) its current response (i) as a function of time (t). (c) Behavior of a triangular potential sweep (v and $-v$) applied to the RC circuit. Plots showing the resultant responses of the circuit as (d) current vs. time and (e) current vs. applied potential.

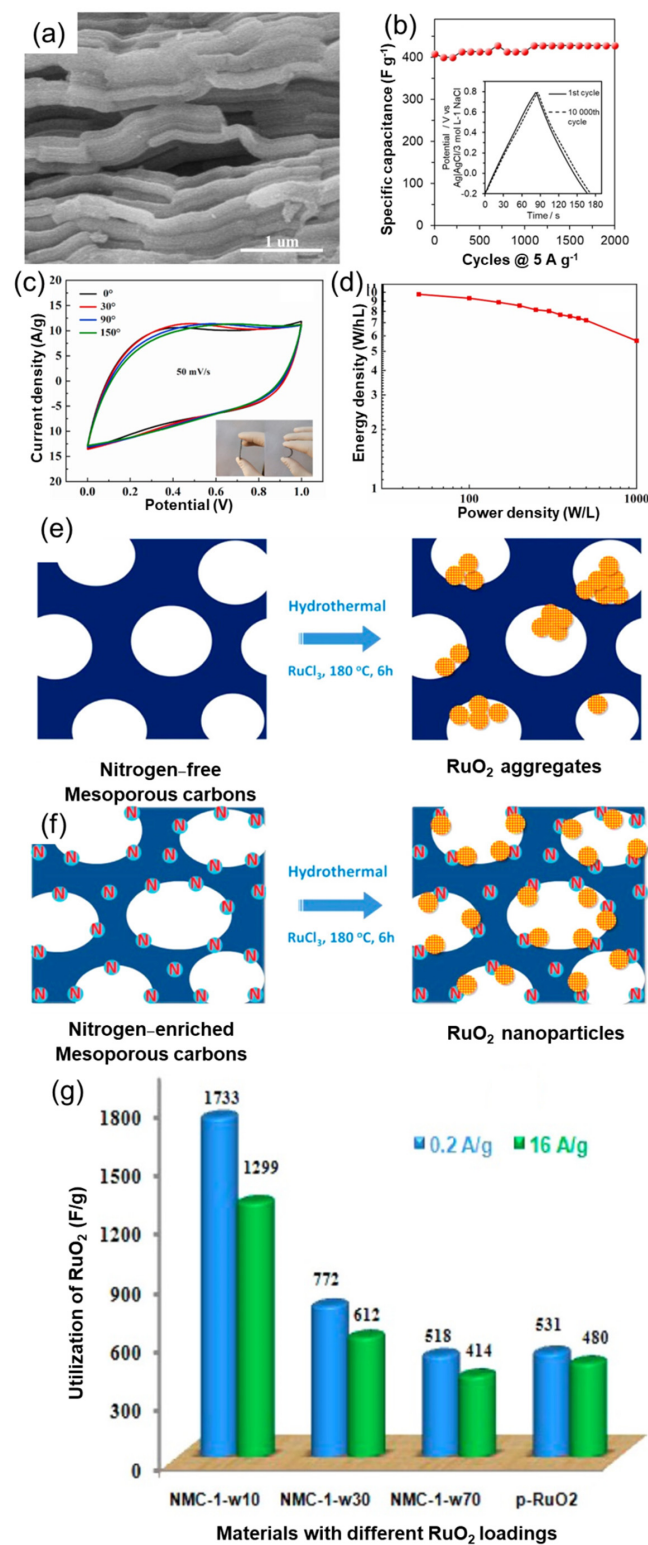


Figure 8. (a) Scanning electron microscopic image of N-doped mesoporous carbon obtained from the silica template method followed by the carbonization [127]. (b) Cyclic stability of activated carbon derived from the chitin biopolymer via polystyrene latex templating method followed by the KOH activation process (inset shows the GCD profile after the cyclic stability experiment) [128]. (c) CV and (d) Ragone plot of flexible supercapacitor fabricated from the biomass-derived carbon/graphene composite material [129]. (e,f) Schematic representation of aggregated as well as evenly distributed RuO₂ nanoparticles over the undoped and N-doped porous carbon structure [131]. (g) 2D plot showing the specific capacitance variations with the different RuO₂ contents.

4.2. Charge Storage Mechanism Based on Pseudocapacitance

The electrode materials that adopt reversible oxidation-reduction reactions (Faradaic processes) at their surface or close to the surface for electrochemical storage are categorized as pseudocapacitive materials [132–135]. The concept of reversible electrochemical adsorption of groups/species over the surface of electrode materials is used to explain the behavior of pseudocapacitance. Furthermore, the kinetic theory of heat of adsorption and the surface coverage is extended to explain the various types of pseudocapacitance, namely ‘adsorption pseudocapacitance’ (for example, adsorption of oxide or hydroxide species on the surface of nickel oxide) and ‘redox pseudocapacitance’ (for example, Faradaic reactions of ruthenium oxide in aqueous electrolytes) [134,136,137]. In all of these cases, the extent of pseudocapacitive processes (surface coverage or redox reactions) linearly depends on the applied potential (V). For instance, in the case of ‘adsorption pseudocapacitance’, let us consider electrochemical adsorption of a cationic species ‘S⁺’ on the surface of electrode material (M) as given in Equation (14). Based on the Langmuir adsorption isotherm, the surface coverage (θ) of ‘MS_{ads}’ is mainly related to the concentration ([S]) and the applied potential (V; Equation (15)).



$$\frac{\theta}{1 - \theta} = k_r \cdot [S] \cdot e^{(\frac{VF}{RT})} \quad (15)$$

where ‘k_r’ is rate constant, ‘F’ is Faraday constant, ‘R’ is gas constant, and ‘T’ is temperature. The Nernst equation, which correlates the equilibrium electrode potential (E) and standard electrode potential (E°) with the concentration of reactive species, could be written as given in Equation (16) by introducing Equation (15) into it. From the above equations, the pseudocapacitance (C_Ø) could mathematically be related to the charge (Q) and the monolayer surface coverage (θ ; Equation (17)).

$$E = E^\circ + \frac{RT}{F} \ln \left[\frac{1}{k_r [S]} \frac{\theta}{1 - \theta} \right] \quad (16)$$

$$C_\varnothing = Q \frac{d\theta}{dV} = \frac{QF}{RT} \cdot \frac{k_r \cdot [S] \cdot e^{(\frac{VF}{RT})}}{(1 + k_r \cdot [S] \cdot e^{(\frac{VF}{RT})})^2} = \frac{QF}{RT} \theta (1 - \theta) \quad (17)$$

From Equation (17), it is predicted that when the surface coverage reaches the value of ‘0.5’, the pseudocapacitance would be maximum for a Langmuir-type electrochemical adsorption process. In some cases, the maximum surface coverage happens in a broader potential range with a slower rate. It is attributed to the increased steric repulsion forces of the adsorbed species upon increasing the surface coverage and also to the multiple electrochemical successive adsorption states. By introducing the parameter of lateral interaction (g_l) (Equation (18)), the pseudocapacitance is expressed based on the Frumkin-type adsorption isotherm (Equation (19)).

$$\frac{\theta}{1 - \theta} = k_r \cdot [S] \cdot e^{(\frac{VF}{RT} - g_l \theta)} \quad (18)$$

$$C_\varnothing = \frac{QF}{RT} \cdot \frac{\theta (1 - \theta)}{1 + g_l \theta (1 - \theta)} \quad (19)$$

The lateral interactions of adsorbed species might be attractive ($g_l > 0$) or repulsive ($g_l < 0$) forces. If it is an attractive force, the maximum surface coverage occurs in a broader potential range, and it is usually lower than that of the Langmuir-type adsorption processes. The other type of ‘redox pseudocapacitance’ is explained by replacing the concept of surface coverage with the concentration of redox species ((Ox) or (Red)). The above thermodynamic relations only correlate the pseudocapacitance with the applied potential. In addition, the investigation of pseudocapacitance on various electrode materials exhibits that it is a highly reversible electrochemical process with an extended time scale and unlimited mass

transfer opportunities. Furthermore, the highly reversible nature of kinetic electrochemical processes is identified by the mirror-imaged cyclic voltammograms and the GCD plots with very minor hysteresis. Some of the pseudocapacitance electrode materials, however, do not show obvious redox (Faradaic) characteristics due to their combination with the EDLC behavior. In these cases, the current response of EDLC is equal to or higher than that of the redox current. Furthermore, they have a very high electrochemically active surface area than that predicted by gas adsorption techniques. On the other hand, in addition to the above interpretations of pseudocapacitance, the battery-like behaviour has also been linked in the mechanistic explanation of pseudocapacitance. As a solution for the above confusion, alternative concepts [132] of ‘linear pseudocapacitance’ (CV with rectangular-shape and GCD with triangular-shape) and ‘non-linear pseudocapacitance’ (where the CV and GCD are deviated from the rectangular- and triangular-shape, respectively) are proposed.

In particular, the transition metal-based compounds are mainly studied for the pseudocapacitance behavior towards the supercapacitors in various electrolyte systems [7]. The ruthenium-based nanocomposite material composed of RuO₂ nanoparticles and the N-doped mesoporous carbon is prepared by the hydrothermal route [131]. The doped nitrogen atoms of the mesoporous carbon evenly distribute the RuO₂ nanoparticles over the porous carbon structures (Figure 8e,f). The nanocomposite material with the ~10 wt% of RuO₂ delivers a very high specific capacitance of 1733 F g^{-d} at 200 mA g^{-a} and a capacity retention of >91% after 2500 cycles (Figure 8g). Similarly, the cobalt oxide (Co₃O₄)/3D carbon structures are prepared via the starch gel method and freeze-drying process followed by the thermal treatment [138]. The Co₃O₄/3D carbon composite exhibits a higher specific capacitance of ~1315 F g⁻¹ at 1000 mA g⁻¹ (Table 1). In the two-electrode configuration, the supercapacitor device with the composite material as the positive electrode and the commercial activated carbon as the negative electrode shows the energy and power densities of ~150 Wh kg⁻¹ and 800 W kg⁻¹, respectively, with better cyclic stability (>91% after 12,000 cycles). Both of the above electrode materials are tested in conventional aqueous electrolyte systems. On the other hand, propylene carbonate (PC)-based nonaqueous electrolyte with 1 M LiClO₄ salt is used for the MoO₃ nanosheets prepared via the solvent exfoliation technique [139]. In a two-cell configuration with the MoO₃ as positive and lithium as negative electrodes, the Li-ion capacitor shows a specific capacitance of ~500 F g⁻¹ at a scan rate of 0.1 mV s⁻¹. Furthermore, the MoS₂-based graphene composite prepared via the ball milling method is tested in an acetonitrile solution of 0.5 M tetraethylammonium tetrafluoroborate (TEA BF₄) [140]. The symmetric two-electrode device exhibits a specific capacitance of ~15 F g⁻¹ at 750 mA g⁻¹ and a capacity retention of >90% after 5000 cycles. The calculated energy and specific power values of the device are >18 Wh kg⁻¹ and 1.12 kW kg⁻¹.

WIS and DES-based electrolytes are also tested for diverse electrode materials, including redox-active polymers [141], transition metal dichalcogenides [142], and their composites [143]. For example, the perylenetetracarboxylic diimide-based redox-active polymers with distinct morphologies are studied in the two different WIS electrolytes such as 27 m potassium acetate (KOAc) and 27 m ammonium acetate (NH₄Ac) systems [141]. The nanomorphologies of the polymers are tuned from the 1D tapes to randomly stacked 2D flakes by utilizing the mono- as well as disulfide linker units, respectively (Figure 9a). The polymer with mono-sulfide linker (PMS) exhibits higher BET surface area and electrical conductivity of 61 m² g⁻¹ and 25 mS m⁻¹. The asymmetric supercapacitor device fabricated with the monosulfide-linked polymer as negative and the activated carbon as positive electrodes exhibits a specific capacitance of 75 F g⁻¹ at 1000 mA g⁻¹ and the capacitance retention of >79% after 10,000 cycles in 27 m KOAc (Table 1). The device energy and power densities are calculated as 22 Wh kg⁻¹ and 8500 W kg⁻¹. The electrochemical performance of the asymmetric supercapacitor is better in the 27 m KOAc WIS electrolyte than that of its ammonium counterpart due to the smaller size and the higher diffusion of potassium ions. The PMS polymer shows a higher surface-controlled process (capacitive) in the KOAc than that of the NH₄OAc due to the faster kinetics (Figure 9b,c). Furthermore,

the 2D layered material, such as a MoS₂-based composite material, is investigated in a DES electrolyte composed of acetamide and LiClO₄ (Figure 9d) [142]. As the DES electrolyte has a higher viscosity and lower ionic conductivity, the physicochemical properties are improved by adding water and acetonitrile in a mole ratio of 1:4.4 (with respect to the salt). The optimum water/acetonitrile-mixed DES electrolyte possesses a better ESW and conductivity of 2.55 V and >15 mS cm⁻¹, respectively (Figure 9e,f). The MoS₂ composite material with the reduced graphene oxide shows a higher specific energy of 31 Wh kg⁻¹ and specific power of ~1200 W kg⁻¹ in a symmetrical two-electrode configuration. After 20,000 cycles, the device retains >90% of its initial capacitance.

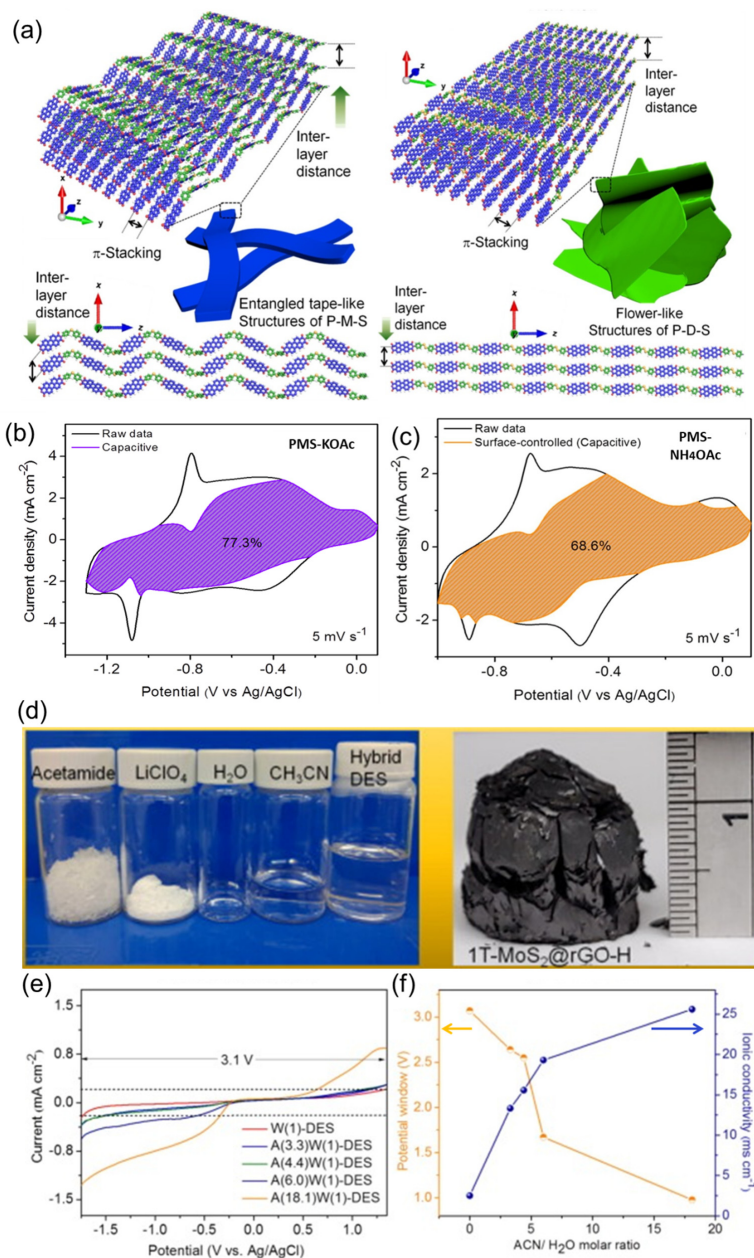


Figure 9. (a) Schematic representation showing the effect of mono- and di-sulfide linkers in the nanomorphology of perylenetetracarboxylic diimide-based redox-active polymers [141]. (b,c) CV with the capacitive (surface-controlled process) contribution of PMS polymer in the 27 m KOAc and 27 m NH₄OAc WIS electrolytes, respectively. (d) Photographs of water/acetonitrile-mixed DES electrolyte and the MoS₂ composite material with the reduced graphene oxide after the freeze-drying process [142]. (e) LSV and (f) ESW (orange line) vs. ionic conductivity (blue line) plots of the water/acetonitrile-mixed DES electrolyte under various conditions.

4.3. Charge Storage Mechanism Based on Battery-like Behavior

The electrode materials that exhibit the electrochemical intercalation behavior (battery-type) have shown significant contributions toward high-performance supercapacitors [144,145]. Though the development of intercalation-based electrode materials was started a decade after the concept of pseudocapacitance was introduced, the actual boundary between these two concepts is blurred, especially for nanostructured materials and the solid–solution intercalation-based materials (no phase transition during the intercalation process). It is due to the very minimal structural transitions of electrode materials upon intercalation when compared to rechargeable batteries, which usually have alloying and phase conversion processes. Later, the concepts of ‘deep’ and ‘shallow’ adsorption of species over the electrode materials are used to explain the charge storage mechanism of intercalating materials [146]. In general, the shallow-adsorption sites are the reaction centers that could easily be reached by the intercalating species (electrolyte ions), whereas the deep-adsorption sites are buried within the material, and are very difficult to access due to the higher activation energy barrier. This process would not happen within the time scale of redox pseudocapacitance. In battery-type materials, the intercalation of ions occurs relatively at a slower rate due to the restrictions on the diffusion process.

Since the layered nanomaterials inherently have accessible interlayer distances, the intercalating species could easily be diffused into the layers, resulting in bulk redox reactions at the active sites. Furthermore, the iron, nickel, and cobalt-based compounds [147–150] generally undergo a diffusion-controlled Faradaic process in aqueous electrolytes with the characteristics of battery-type electrode material. For example, the Prussian blue analog of cobalt-based framework structure is tested in a 0.5 M Na₂SO₄ electrolyte towards sodium-ion supercapacitor [147]. The cobalt hexacyanoferrate (Co-Fe-HCF) complex with nanoparticle morphology has several empty sites of ferricyanide that induce defects in the 3D bimetallic cubic framework structure. The nanoparticles with an average size of 20 nm are fused to form the interconnected structure with higher porosity (BET surface area of 434 m² g⁻¹). In a three-electrode configuration, the complex exhibits the specific capacitance of 250 F g⁻¹ at 1000 mA g⁻¹ (Table 1). The GCD plots show a clear potential plateau (Figure 10a) in the range of 0.35 to 0.55 V vs. SCE, due to the diffusion of sodium ions into the framework for the bulk redox reactions (Fe (II)/Fe (III)), which is a characteristic of battery-type material (Figure 10b). It also shows better cyclic stability of >90% capacitance retention after 5000 cycles. The asymmetric supercapacitor device fabricated with the cobalt hexacyanoferrate as the positive electrode and the graphene as the negative electrode possesses the energy and power densities of 34 Wh kg⁻¹ and 2500 W kg⁻¹. Furthermore, the additive-free electrode composed of electrodeposited NiSe nanoparticles over the CVD-grown carbon nanotubes (Figure 10c) on stainless steel current collector is tested in alkaline electrolytes of different metal ions (Li⁺, Na⁺ and K⁺) [151]. The carbon nanotubes serve as a better channel to transport the charges to the current collector, and the NiSe nanoparticles act as battery-type material. In the strong alkaline medium, the NiSe is converted into Ni(OH)₂, and the bulk reversible redox reaction of Ni(OH)₂ into NiOOH is responsible for the Faradaic processes (Figure 10d). Among the three alkaline electrolytes, the NiSe/CNT composite shows superior electrochemical performances in the 3 M LiOH with the specific capacitance of 1007 F g⁻¹ at 1000 mA g⁻¹ under a three-electrode configuration (Table 1). The smaller size and the better diffusion of lithium ions might be attributed to better electrochemical performances than that of the sodium and potassium ions. The hybrid supercapacitor device composed of the NiSe/CNT (positive electrode) and the reduced graphene oxide (negative electrode) shows a specific capacity of 39 mAh g⁻¹ at 1000 mA g⁻¹, and the energy and power densities of 32 Wh kg⁻¹ and 823 W kg⁻¹. In addition, a redox-active polymer with mixed amine groups is also employed as battery-type electrode material for the supercapacitor application [152]. A fused nanoparticle-like structure of mixed amines-containing (aniline and triphenyl aniline) copolymer is formed from the random arrangement of branched-chain polymeric units. In a superconcentrated WIS electrolyte (30 m NH₄OAc), an all-organic

supercapacitor is assembled with a mixed-amine copolymer as the positive electrode and a perylenetetracarboxylic diimide-based polymer as the negative electrode (Figure 10e). The device possesses a wider cell operational potential of up to 1.9 V and a cell capacity of 42 mAh g^{-1} at 200 mA g^{-1} (Figure 10f; Table 1). The electrode kinetics of mixed-amine copolymer is further investigated in a three-electrode configuration. The contribution of the diffusion-controlled process (battery-type behavior) to the total charge storage is calculated from the cyclic voltammograms (Figure 10g) as >77% at the scan rate of 1 mV s^{-1} . The higher percentage of the diffusion-controlled process (Figure 10h) is mainly attributed to the intercalation of ammonium ions into the nanoparticle structures and the reversible conversion of benzenoid to quinoid structures of amine functionalities.

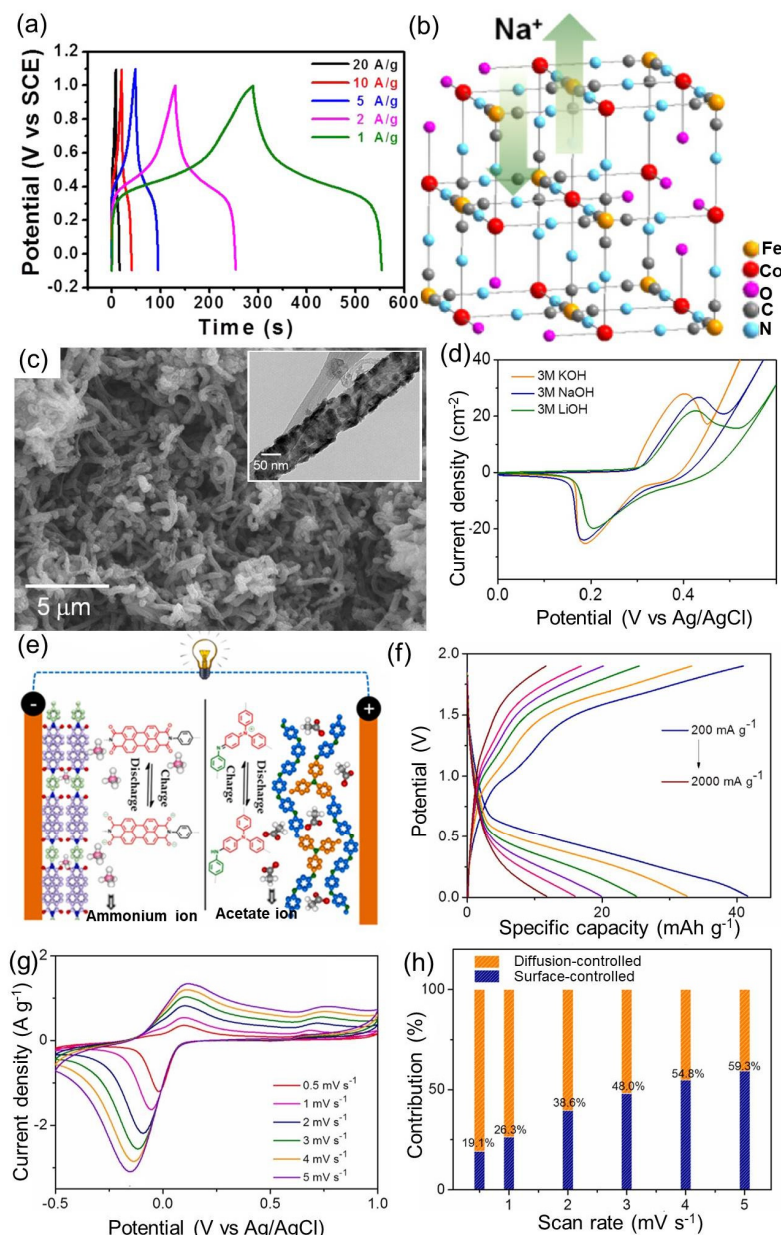


Figure 10. (a) GCD plots of cobalt hexacyanoferrate (Co-Fe-HCF) complex in a $0.5 \text{ M Na}_2\text{SO}_4$ electrolyte [147]. (b) Structure of Co-Fe-HCF with the defects in the framework. (c) Scanning electron and transmission electron microscopic images and (d) the CV (in various alkaline electrolytes) of NiSe/CNT composite [151]. (e) Schematic representation and (f) GCD profiles of all-organic supercapacitor device fabricated from the mixed amine-containing copolymer [152]. Plots of (g) CV and (h) diffusion-controlled contribution of the mixed amine-containing copolymer.

Table 1. Representative examples of various electrode materials and their electrochemical performances.

S. No.	Electrode Material	Electrolyte	Specific Capacitance (F g ⁻¹) at Specific Current (mA g ⁻¹)	Cyclic Stability (no. Cycles)	Specific Energy (Wh kg ⁻¹)/ Specific Power (W kg ⁻¹)/
EDL-capacitive materials					
1.	N-doped mesoporous carbon [127]	0.5 M H ₂ SO ₄	428/250	>98% (20,000)	11/~250
2.	Activated Carbon (Chitin/Polystyrene) [128]	1 M H ₂ SO ₄	567/500	>73% (10,000)	—
3.	Porous carbon/RGO [129]	1 M H ₂ SO ₄	775 (F cm ⁻³)/500	>93% (10,000)	~10 W h L ⁻¹ /61 W L ⁻¹
4.	Porous carbon [130]	EMIMBF ₄ /TEP (ionic liquid)	53/500	>86% (10,000)	43/12
Pseudocapacitive materials					
5.	RuO ₂ /N-doped carbon [131]	1 M H ₂ SO ₄	1733/200	>91% (2500)	—
6.	The Co ₃ O ₄ /3D carbon [138]	3 M KOH	~1315/1000	>91% (12,000)	~150/800
7.	Few layered MoS ₂ [140]	0.5 M TEA BF ₄	~15/750	>90% (5000)	>18/1125
8.	Redox-active polymer (PMS) [141]	27 m KOAc (WIS)	75/1000	>79% (10,000)	22/8500
9.	MoS ₂ -RGO [142]	Acetamide-LiClO ₄ (DES)	42/1000	>90% (20,000)	31/1200
Battery-type materials					
10.	Co-Fe-HCF [147]	0.5 M Na ₂ SO ₄	250/1000 *	90% (5000)	34/2500
11.	NiSe/CNT [151]	3 M LiOH	1007/1000 *	>75% * (500)	32/823
12.	Mixed amine-containing copolymer [152]	30 m NH ₄ OAc	42 mAh g ⁻¹ /200	60% (2000)	>16/79

'M' is molarity (mol L⁻¹) and 'm' is molality (mol kg⁻¹); '*' indicates the value obtained from the three-electrode configuration.

4.4. Investigation of Electrochemical Kinetics by Differentiating Pseudocapacitance and Battery-like Behaviors

An in-depth understanding of charge storage mechanisms paves new insights and helps to attain advanced methodologies for the design of high-performance supercapacitors. In general, the pseudocapacitance is identified by the reversible redox reactions that occur at or near the surface, whereas the electrochemical intercalation process (deep-adsorption followed by the charge-transfer reactions) is categorized as battery-type behavior [153]. The electrochemical characterization technique, such as cyclic voltammetry, is crucial to investigate the kinetics of electrode processes. The mirror-imaged, very broad redox peaks during the forward and reverse CV scans are the important features that distinguish the pseudocapacitive materials from the battery-type behavior. Furthermore, the efficient pseudocapacitive materials do not show much change in the position of redox peaks when the CV scan rate is varied; however, the peak separation increases at a higher scan rate if there are Ohmic losses. In addition, the charge storage efficiencies of these materials are higher even with shorter charge–discharge time scales. The peak current (*i*) of the redox reactions at a particular potential (V) is mathematically related to the scan rate (*v*) as given in Equation (20) (where *a* and *b* are constants). From the value of the constant (*b*) that depends on the scan rate, the contribution of surface-controlled (capacitive) and diffusion-controlled processes are quantitatively evaluated from the slope of the log (*i*) vs. log (*v*) plot; (*i*) when the value of '*b*' is equal to 1, the peak current is directly proportional to the scan rate and it is surface-controlled kinetics. At this condition, the current response is observed due to the formation of an electrical double layer (Equation (21)) or the surface-confined Faradaic reactions (Equation (22)).

$$i(V) = av^b \quad (20)$$

$$i = C_{EDL} \cdot A \cdot v \quad (21)$$

$$i = \frac{nF^2}{4RT} \cdot A \cdot \Gamma \cdot v \quad (22)$$

where ' C_{EDL} ' is EDLC, ' A ' is electrochemically active surface area, ' n ' is the number of electrons transferred and ' Γ ' is the amount of redox-active species that are adsorbed at the surface. However, the above relationship does not differentiate the EDLC from the surface-confined Faradaic reactions (pseudocapacitance) and the value of ' b ' is equal to 1 for both cases. In order to distinguish them, a different approach, such as the evaluation of the electrochemically active surface area, needs to be adopted, and then the EDLC is calculated from the measured surface area and the constant value of $10\text{--}40 \mu\text{F cm}^{-2}$. Nevertheless, the estimation of the actual electrochemically active surface area is difficult for certain pseudocapacitive materials (for example, ruthenium oxide), which have interlayers or grain boundaries that are usually higher than that obtained by the physical gas adsorption experiments. Therefore, the combination of electrochemical characterizations with the *in situ* techniques that detect the charge transfer processes by monitoring the optical or electronic properties should be utilized to differentiate the Faradaic and non-Faradaic processes. (ii) When the value of ' b ' is equal to 0.5, the electrode processes are dominated by the diffusion-controlled kinetics that are usually governed by the Randles–Sevcik relation (Equation (23)).

$$i = 0.4958 \cdot n \cdot F \cdot A \cdot C^* \cdot \sqrt{\frac{D \cdot \alpha \cdot nF \cdot v}{RT}} \quad (23)$$

where ' C^* ' is a concentration of redox-active species, and ' α ' is a transfer coefficient. Equation (23) could be used to investigate the diffusion-controlled processes of electrode kinetics when the diffusion length is largely higher than the value of ' $\sqrt{Dt_d}$ '. (iii) When the value of ' b ' lies between 0.5 and 1, the charge storage mechanism is the combination of both surface- and diffusion-controlled kinetics with a diffusion length that is lesser than the value of ' $\sqrt{Dt_d}$ '. At this condition, the total current response of the electrode material at a particular potential and scan rate ($i_{V,v}$) is deconvoluted into the capacitive and Faradaic processes by using the relationship with the constants ' k_1 ' and ' k_2 ' (Equations (24) and (25)). Upon calculating the values of ' k_1 ' and ' k_2 ' at a particular voltage for the different scan rates, the percentages of surface- and diffusion-controlled contributions to the total current response are quantified. Furthermore, if the electrode material displays larger Ohmic losses at higher scan rates ($>10 \text{ mV s}^{-1}$), the shifting of the redox peaks can be accounted for through this approach. In that situation, another electrochemical characterization technique, such as the potentiostatic-intermittent titration (PIT) method based on the multi-step chronoamperometric technique, is used. In a typical PIT experiment, every applied potential is kept until the equilibrium is reached, and the resultant current response is measured at short time intervals. The effect of Ohmic loss in the estimation of surface- and diffusion-controlled contributions is minimum in this technique as the current response is measured at steady-state conditions.

$$i_{V,v} = k_1(V) \cdot v + k_2(V) \cdot \sqrt{v} \quad (24)$$

$$\frac{i_{V,v}}{\sqrt{v}} = k_1(V) \cdot \sqrt{v} + k_2(V) \quad (25)$$

5. Supercapacitors for Next-Generation Applications

Electrochemical energy storage devices with smart functionalities such as stimuli-responsiveness, real-time monitoring, self-charging, self-protection, and self-healing properties have attracted a lot of attention as they play a crucial role in the development of next-generation devices [154]. Furthermore, smart energy storage devices can spontaneously identify the abnormalities in their functions at the initial stages and provide an

opportunity to implement the rectification process. Supercapacitors are more suitable to incorporate these smart functionalities due to their simple device structure, higher specific power, and ultra-cyclic stability. In addition, the fabrication of smart supercapacitors with great flexibility makes them more adaptable to a wide range of applications, including wearable electronics [155,156], real-time healthcare devices [157], lightweight electronics [158], and aeronautics [159,160].

5.1. Stretchable/Wearable Supercapacitors

Stretchability is an essential property in employing supercapacitor devices for wearable electronics that deform their shape based on the part of our body (hand, chest, and so on) and the external strains during motion [161]. The stretchability can be implemented either via the ‘material design’ or by the ‘device architecture’. The elastomeric substrates with the intended geometry usually impart great flexibility to the supercapacitors. In the material aspects, the components of the device, that is, mainly the electrode and electrolyte materials, should possess better mechanical properties such as Young’s modulus, tear resistance, and elasticity [162]. In addition, the electrochemical performances should not vary much upon mechanical motions and elongation/compression stress. Carbon nanomaterials such as carbon nanotubes and graphene and conducting polymer-based materials are highly preferable electrode materials due to their better mechanical and chemical properties [163]. Elastomeric materials such as poly(dimethylsiloxane) [164] and polyacrylamides [165] are utilized for conventional electrode materials that have poor mechanical properties and stability. For instance, the composite elastomeric material composed of polyaniline and alpha cyclodextrin-functionalized polyacrylamide shows excellent flexibility (Figure 11a). Furthermore, the composite material has a higher porosity and extended interconnected structures with a pore size of ~200 nm (Figure 11b). Because of the higher surface area and electrical conductivity of the composite, the stretchable supercapacitor device exhibits very stable charge storage behavior upon external deformation and elongation stress. (Figure 11c). Furthermore, the carbon nanotube-grown paper substrate with the electrodeposited polypyrrole (CNT/PPy) is employed to fabricate an ultra-flexible and wearable supercapacitor device. The acrylamide-containing polyelectrolyte is incorporated within the device to achieve stretchability up to the strain of 1000% (Figure 11d). The capacitance of the device shows >2-fold improvement upon 1000% of tensile strain, and it is attributed to the enhanced contacts of active material with the electrolyte ions (Figure 11e). On the other hand, the device retained ~99% of its initial capacitance upon the compressional strain (Figure 11f). For stretchable/wearable devices, the physical state of the electrolyte should be stretchable semi-solid/solid materials to prevent leakage upon elongation/compression stress [166,167]. Poly (vinyl alcohol), poly(vinylidene fluoride), poly(acrylic acid), poly(methyl methacrylate), and poly(ethylene oxide) are commonly used to prepare flexible electrolyte media for stretchable supercapacitors [168]. The flexibility of these electrolytes is further improved by employing the post-crosslinking processes by interconnecting more and more links towards better stability [169]. From device architectural aspects, various fabrication techniques such as spray/dip coating, chemical/electro-deposition, and layer-by-layer assembly are used to attain better flexibility [170–173]. Furthermore, structural modification techniques such as folding and cutting methods are also utilized to provide stretchability to the devices [174,175].

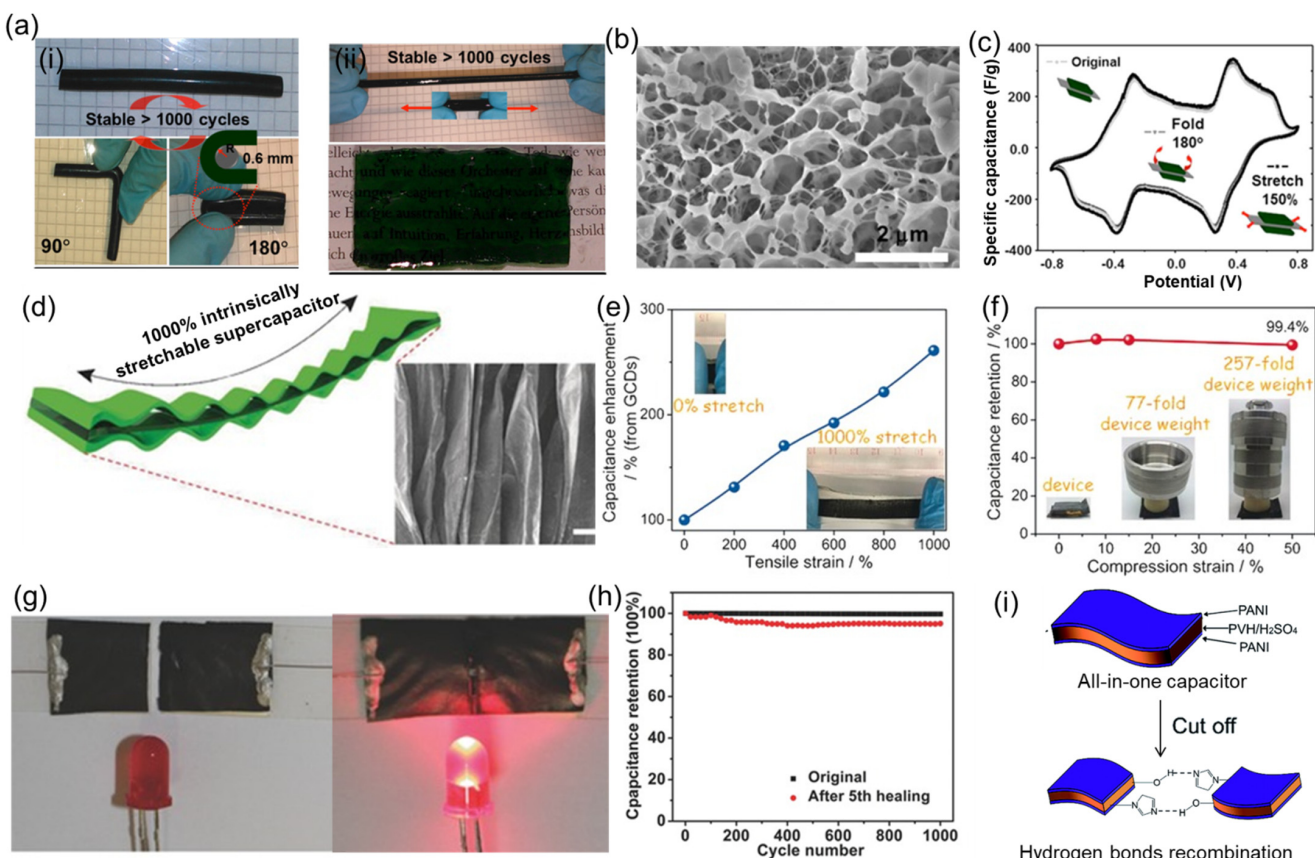


Figure 11. (a) Photographs showing the stretchable electrode material composed of polyacrylamide and polyaniline upon (i) bending and (ii) elongation conditions [165]. (b) Scanning electron microscopic (SEM) image of the polyacrylamide and polyaniline-based electrode material. (c) CV of the stretchable supercapacitor fabricated with the polyacrylamide and polyaniline composite. (d) SEM image of polypyrrole deposited over the carbon nanotube-based paper substrate (PPy-CNT). The capacitance changes in CNT-PPy-based stretchable supercapacitor upon (e) tensile and (f) compression strains [167]. (g) Photographs and (h) cyclic stability of self-healing supercapacitor based on SWNT electrode material and TiO₂ incorporated polyamide substrate before and after the self-healing process [176]. (i) Schematic representation showing the self-healing process of PANI/PVH/H₂SO₄-based supercapacitor via recombination of hydrogen bonding interaction [177].

5.2. Self-Healing Supercapacitors

The introduction of smart properties such as self-protection and self-healing to the supercapacitor devices increases the performance and lifetime with reduced cost and environmental issues [178]. The self-healing supercapacitors repair any fracture or puncture on their own due to severe mechanical stress and prevent sudden performance loss. The self-healing properties are usually imparted by incorporating the self-healable polymer networks into the device architecture. They utilize dynamic intermolecular interactions, namely hydrogen bonding, disulfide bonds, and host–guest interactions, to attain self-healing behavior. Polyurethanes and poly(dimethylsiloxane)-based polymeric materials are employed for this purpose [179,180]. Certain polymeric materials require external reagents to initiate the healing process, and they should be stored within the device for delivery on demand [181]. In general, carbon-based materials are coated on the self-healing polymeric substrate and used to fabricate the supercapacitor. For example, the carbon nanotubes are deposited over the polyamide substrate with conductive TiO₂ nanoparticles and used as self-healable electrode material for supercapacitor fabrication [176]. The device shows excellent self-healing behavior upon cutting and subsequent healing events (Figure 11g). The specific capacitance of the device possesses > 85% retention after five cycles of self-

healing cycles (Figure 11h). In another example, a self-healable supercapacitor comprising of the electrode material (a combination of nickel particles, eutectic liquid of gallium-indium and polyurethane) and the ionic liquid electrolyte (1-Butyl-3-methylimidazolium bis(trifluoromethyl sulfonyl)imide) shows higher conductivity even at a 700% strain and retention of 76% after several cycles of self-healing process achieved via dynamic hydrogen bonding and the conductivity restoration with the liquid metal [182]. In addition, a copolymer electrolyte consisting of vinyl imidazole and hydroxypropyl acrylate units and sulfuric acid (PVH/H₂SO₄) serves as a self-healable electrolyte system (Figure 11i). The supercapacitor device fabricated with the copolymer electrolyte and the pseudocapacitive polyaniline (PANI) flakes retains the areal capacitance of 367 mF cm⁻² after ten cycles of self-healing cycles from its initial capacitance of 403 mF cm⁻² [177].

5.3. Self-Charging Supercapacitors

For the continuous operation of wearable electronics and real-time health monitoring devices, the integrated energy storage device needs to be recharged instantaneously with an external power source, which has practical difficulties in some scenarios [183]. It should be addressed in the advanced next-generation health monitoring devices. The integration of energy harvesting characteristics into the supercapacitor smartly addresses the above-mentioned issue, and it further decreases the complexity of wearable electronics. The incorporation of nanogenerators that convert various forms of mechanical energy into electrical energy is the best approach for this purpose. Several piezo (stress into electricity), tribo (friction into electricity), and thermoelectric (heat into electricity) materials are utilized to prepare the electrode materials to impart the energy harvesting characteristics [184,185]. For example, a self-charging supercapacitor is fabricated with the functionalized polyvinylidene fluoride polymer as piezoelectric material with the polyvinylalcohol/sulfuric acid electrolyte (Figure 12a) [186]. When a compressive strain is applied, the change in remnant polarization of PVDF film drives the redistribution of ions across the device, which leads to the generation of piezo potential (Figure 12b). A self-charging of 100 mV is achieved within 40 s upon the continuously applied force (at 4.5 Hz). Furthermore, the self-charging ability of the supercapacitor device is improved by compositing polyvinylidene fluoride polymer with sodium niobate, which attains a voltage of 680 mV with the force of 25 N in 100 s of self-charging time [187]. The self-charging of the supercapacitor from the thermal gradient across the device (top and bottom electrodes) is observed by incorporating the thermoelectric polymer electrolyte [188]. The mixture of polyethylene oxide with sodium hydroxide possesses the Seebeck coefficient of +11.1 mV K⁻¹. The assembled supercapacitor attains a voltage of 180 mV from the temperature gradient of 16 K (Figure 12c).

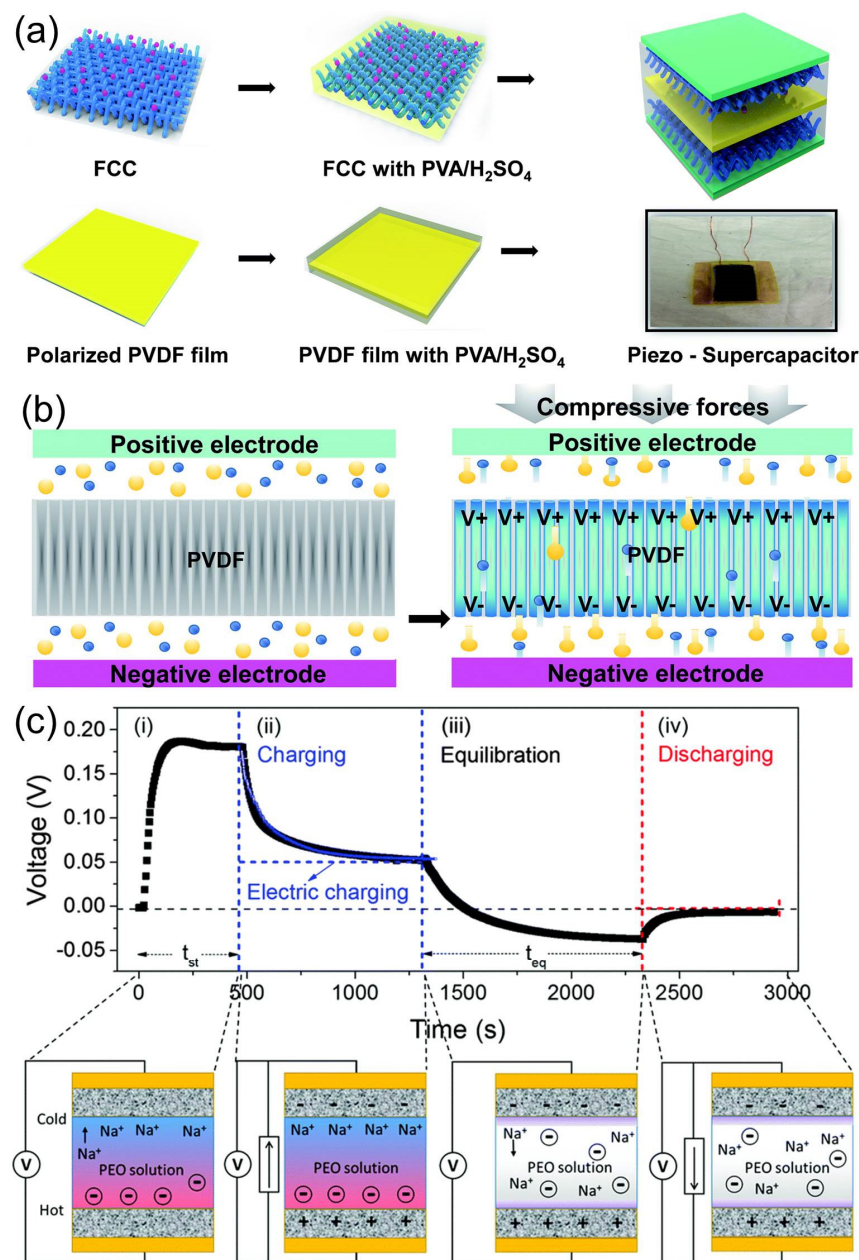


Figure 12. (a) Fabrication and (b) working mechanism of piezoelectric-based self-charging supercapacitor composed of PVDF film and PVA/H₂SO₄ polymer electrolyte over the carbon cloth substrate [186]. (c) Galvanostatic charge–discharge profile (at different conditions such as (i) initial, (ii) charging, (iii) equilibration & (iv) discharging stages) and the working mechanism of thermoelectric-based self-charging supercapacitor fabricated from the polyethylene oxide-sodium hydroxide electrolyte and CNT-based electrode materials [188].

6. Summary and Outlook

The high-performance supercapacitor is an inevitable candidate to tackle the present and future global energy crises. In order to fulfill the need for superior energy storage capabilities for rapid technological developments, significant amendments are essential in the various aspects of the supercapacitor devices, which include the components, device architecture, evaluation, and diagnostic methods. In this review, the overview of most of these aspects is comprehensively discussed. The electrode and electrolyte materials are the heart of the energy storage devices, and they predominantly determine the overall performance. For example, the specific capacitance, power density, and energy density of a

device mainly depend on the electrical conductivity, electrochemically active surface area, and chemical stability of electrode material, as well as the size of charge carriers, ionic conductivity, viscosity, boiling point, and electrochemically stable potential window (ESW) of the electrolyte. Among the various electrode materials developed, the extensively exploited materials are porous carbon (activated carbon and mesoporous carbon), 1D and 2D carbon nanomaterials (carbon nanotubes and graphene), transition metal-based compounds (oxides, sulfides, and nitrides), 2D layered materials (MXenes, dichalcogenides, and double hydroxides), redox-active polymers (conducting polymers and conjugated/unconjugated polymers with carbonyl/imide/radical moieties), and metal-organic and covalent organic frameworks. The electrochemical performances of these electrode materials are often intrinsically tuned by modulating the crystallinity, defect structures, and surface morphology (nanostructuring) as well as extrinsically by doping and compositing/hybridizing with other components/materials to attain superior charge storage characteristics. The different crystalline phases of a particular material exhibit distinct electrochemical properties, and the optimization of these polymorphic phases results in improved redox activities. Furthermore, the introduction of chemical or structural imperfections (defects) affects the electronic properties such as the bandgap, charge carrier concentration, work function, and electrical conductivity, which in turn influence the surface activities of the electrode materials. Similarly, the tuning of surface morphology is crucial to control the electrochemically active surface area and the charge carrier transport. The electrode materials with multi-dimensional (0D–3D) nanomorphologies (nanoparticles, fibers, sheets, and flower-like structures) usually show superior electrochemical characteristics due to the more exposed active sites and the shorter diffusion length. In addition, the charge storage properties of poorly performing electrode materials are improved by doping or preparing composites/hybrids with other materials that significantly increase the electrical conductivity and redox activity at the electrode–electrolyte interfaces. Carbon nanomaterials, such as carbon nanotubes, graphene, and reduced graphene oxide, are commonly used materials to achieve composite electrode materials towards higher-performance supercapacitors.

The electrolytes used for the supercapacitor device are broadly categorized as conventional (aqueous and nonaqueous/organic solvent-based) and unconventional (ionic liquids (ILs), water-in-salt (WIS), deep-eutectic solvents (DES)) electrolytes. Acidic (sulfuric, hydrochloric, and phosphoric acids), alkaline (lithium, sodium, and potassium hydroxide), and neutral salt (sulfates, chlorides, and phosphates) solutions in water are examples of aqueous electrolyte systems. The major limitation of the aqueous electrolyte is narrow ESW due to the water decomposition reaction over the positive and negative electrodes if the operating potential range (V) is higher than 1.23 V, which subsequently leads to a lower specific energy. The electrolysis of water can effectively be suppressed by adjusting the pH, introducing redox additives, and increasing the concentration (WIS electrolyte). On the other hand, the modifications of the electrode surface, such as doping of alkali ions, optimization of electrode mass ratio, and tuning of surface charge density, also lower the extent of the water decomposition reaction. WIS and DES-based electrolytes are better alternatives to aqueous electrolytes with lower ESW. The WIS electrolytes are the super-concentrated salt solutions (21 molal (m) LiTFSI, 17 m NaClO₄, and so on, and even dual-ion-based WIS) in which the fraction of free water molecules is very low, and most of them are strongly bound with the cation and anions of the metal salts. The IL- and DES-based electrolytes generally have wider ESW, thereby providing higher specific energy to the supercapacitor devices. However, they badly suffer from high viscosity and low ionic conductivity when compared to aqueous electrolytes. The additional water or other organic solvents (propylene carbonate/acetonitrile) is employed to improve the ionic conductivity of the ILs and DES-based electrodes by slightly compromising the ESW. Though the WIS electrolytes provide wider ESW, they are expensive and hinder their use for commercial applications. Alternatively, the cheaper salt substitutes should be achieved with higher ionic conductivity and lower viscosity towards the high-performance electrolyte systems. Furthermore, the electrode materials could be covered with an ionically conductive as

well as electrically insulating solid–electrolyte interphase (SEI) that effectively lowers the activity of water over the electrode surface. The SEI coatings with superior physicochemical characteristics (high porosity and ion permeability) should be developed, while a few have already been employed for this purpose. In addition to electrode and electrolyte materials, the other components of the supercapacitor, such as conductive additives (carbon black), polymer binders (PVDF, PTFE, and Nafion), and current collectors (foil, foam, and mesh of Cu/Al/Ti/Ni and carbon fabric) also influence the charge storage characteristics of the device. The purpose of binders and conductive additives is to ensure the interconnectivity and efficient charge percolation of the electrode materials. The particle size and the mixing ratio of the additives are crucial to attain maximum porosity and electrolyte access. The major challenge of retaining close contact between the electrode materials and the additives could substantially be addressed by better mixing procedures and composite formations, such as the cosynthesis of electrode material with highly conductive carbon structures.

Understanding the charge storage mechanism often leaves major clues to reinventing high-performance components and unprecedented device architectures. For instance, the detailed investigations and the continuous tuning of pseudocapacitive behavior provided an opportunity to adopt the intercalation battery-type chemistry into the Faradaic processes of the supercapacitors. Furthermore, the supercapacitors mainly focusing on the charge transfer mechanisms at the electrode–electrolyte interface though the batteries primarily deal with the phase transitions and diffusions in the solid state. The substantial collaboration of computational-guided materials development and the versatile *in situ* characterization techniques enables the deep realization of electrical double layer and charge transfer processes at the atomic level. It would strengthen not only the fundamentals of charge storage, but also the technological inventions in the electrochemical interfacial processes. The integration of electrode characteristics (electronic and surface properties) with the electrolyte environment in dynamic as well as self-consistent fashions is key to developing atomic-level simulation models for the electrode–electrolyte interfaces. These models would provide crucial insights into the response of electrodes in a particular electrolyte to the applied potential in terms of lattice parameters, redox states, and site possessions. Then, the material design and syntheses could computationally be guided by these models at first, and the optimized device components would be attained towards the high-performance device fabrications. In addition, unprecedented *in situ* techniques would also be able to verify those processes and provide inputs for remodifications. The *in situ* techniques, which are integrated with the suitable characterization methods, should be able to follow the electrochemical processes at the time scales relevant to the particular charge storage mechanism. For example, the electrochemical quartz crystal microbalance would identify the characteristics of absorbed/diffused species that are responsible for the charge storage behavior. Furthermore, structural transformations are inevitable due to the insertion and distribution of ions into the material during the charge transfer events. The Raman and Infrared spectroscopies are crucial to detect the local structural transitions. The synchrotron X-ray absorption and diffraction techniques (XRD and XAS) could be able to detect the structural dynamics as well as to distinguish even the multiple redox couples during the complex electrode kinetics. Scanning electron microscopy could also be used to trace the mechanical deformations of the electrode materials in spatial resolutions. In addition, electro-optical microscopy integrated with step-potential electrochemical spectroscopy could be utilized to characterize the smart supercapacitors (self-charging/self-healing devices) by measuring the ion concentrations with the help of optical density variations. Beyond the performance improvements in the supercapacitor’s components, the energy management protocols should also be imposed rigorously for high-end aeronautical applications such as fully electric aircraft. For example, the implementation of a large-scale supercapacitor device greatly reduces the overload of the main aircraft generator for a few minutes through the centralized smart controller facility. Furthermore, a state-of-the-art integrated and fully controlled supercapacitor device also helps to smoothen the aircraft generator power profile by absorbing the power peak of electro-mechanical actuators or

delivering the stored energy toward the power overload. In the near future, we need more substantial collaborations of numerous techniques and approaches to achieve optimistic device components and architectures towards high-performance next-generation supercapacitors to fulfill our ceaseless energy demands.

Author Contributions: Conceptualization, methodology, investigation, validation, writing-review and editing, supervision K.C.S.L.; Conceptualization, methodology, investigation, validation, writing-review and editing, supervision, B.V. All authors have read and agreed to the published version of the manuscript.

Funding: This research received no funding.

Data Availability Statement: Some figures of this review are reproduced from the previously published articles. However, the proper copyright permissions were obtained through the “CCC Rightslink”. Figure 3a—Licence 5475180864978, 24 January 2023; Figure 5b—Licence 547580444590; Figure 5c—Licence 5475181238052; Figure 5d,e—Licence 547590036090, 24 January 2023; Figure 8a—Licence 5475210332988, January 24, 2023; Figure 8b—Licence 547510560650, 24 January 2023; Figure 8c,d—Licence 5475210751661, 24 January 2023; Figure 8e—g (permission was granted by the American Chemical Society; a licence number was not generated from the system, 24 January 2023); Figure 9a—c—Licence 5475211356094, 24 January 2023; Figure 9d—f—Licence 5475230046030, 24 January 2023; Figure 10a,b (permission was granted by the American Chemical Society; a licence number was not generated from the system, 24 January 2023); Figure 10c,d—Licence 5475251355213, 24 January 2023; Figure 10e—h—Licence 5475260101791, 24 January 2023; Figure 11a—c (permission was granted by the American Chemical Society, a licence number was not generated from the system, 24 January 2023); Figure 11d—f—Licence 5475260510527, 24 January 2023; Figure 11g,h—Licence 5475260706021, 24 January 2023; Figure 11i—Licence 1315164-1, 24 January 2023; Figure 12a,b—Licence 1315166-1, 24 January 2023; Figure 12c—Licence 1315166-2, 24 January 2023.

Acknowledgments: B.V. acknowledges the ‘Japan Society for the Promotion of Science’ for the research fellowship (P21035). K.C.S.L. acknowledges ‘Chiba University’ for the research fellowship.

Conflicts of Interest: The authors declare no conflict of interest.

References

1. Liu, J.; Zhang, J.-G.; Yang, Z.; Lemmon, J.P.; Imhoff, C.; Graff, G.L.; Li, L.; Hu, J.; Wang, C.; Xiao, J.; et al. Materials Science and Materials Chemistry for Large Scale Electrochemical Energy Storage: From Transportation to Electrical Grid. *Adv. Funct. Mater.* **2013**, *23*, 929–946. [[CrossRef](#)]
2. Yu, Z.; Tetard, L.; Zhai, L.; Thomas, J. Supercapacitor electrode materials: Nanostructures from 0 to 3 dimensions. *Energy Environ. Sci.* **2015**, *8*, 702–730. [[CrossRef](#)]
3. Helmholtz, H. On some laws of the distribution of electric currents in physical conductors with application to animal electrical experiments. *Ann. Phys.* **1853**, *165*, 211–233. [[CrossRef](#)]
4. Becker, H.E. Low Voltage Electrolytic Capacitor, General-Electric 2 800 616. 1957. Available online: <https://patents.google.com/patent/US2800616A/en> (accessed on 24 January 2023).
5. Treacy, E.A. NEC Corporation. Encyclopedia Britannica. 2020. Available online: <https://www.britannica.com/topic/NEC-Corporation> (accessed on 25 January 2023).
6. Bullard, G.L.; Sierra-Alcazar, H.B.; Lee, H.L.; Morris, J.L. Operating principles of the ultracapacitor. *IEEE Trans. Magn.* **1989**, *25*, 102–106. [[CrossRef](#)]
7. Choi, C.; Ashby, D.S.; Butts, D.M.; DeBlock, R.H.; Wei, Q.; Lau, J.; Dunn, B. Achieving high energy density and high power density with pseudocapacitive materials. *Nat. Rev. Mater.* **2020**, *5*, 5–19. [[CrossRef](#)]
8. Yu, F.; Huang, T.; Zhang, P.; Tao, Y.; Cui, F.-Z.; Xie, Q.; Yao, S.; Wang, F. Design and synthesis of electrode materials with both battery-type and capacitive charge storage. *Energy Storage Mater.* **2019**, *22*, 235–255. [[CrossRef](#)]
9. Vlad, A.; Singh, N.; Rolland, J.; Melinte, S.; Ajayan, P.M.; Gohy, J.F. Hybrid supercapacitor-battery materials for fast electrochemical charge storage. *Sci. Rep.* **2014**, *4*, 4315. [[CrossRef](#)]
10. Dubal, D.P.; Ayyad, O.; Ruiz, V.; Gómez-Romero, P. Hybrid energy storage: The merging of battery and supercapacitor chemistries. *Chem. Soc. Rev.* **2015**, *44*, 1777–1790. [[CrossRef](#)]
11. Zhang, X.; Jiang, C.; Liang, J.; Wu, W. Electrode materials and device architecture strategies for flexible supercapacitors in wearable energy storage. *J. Mater. Chem. A* **2021**, *9*, 8099–8128. [[CrossRef](#)]
12. Guo, X.; Zheng, S.; Zhang, G.; Xiao, X.; Li, X.; Xu, Y.; Xue, H.; Pang, H. Nanostructured graphene-based materials for flexible energy storage. *Energy Storage Mater.* **2017**, *9*, 150–169. [[CrossRef](#)]

13. Liang, T.; Hou, R.; Dou, Q.; Zhang, H.; Yan, X. The Applications of Water-in-Salt Electrolytes in Electrochemical Energy Storage Devices. *Adv. Funct. Mater.* **2021**, *31*, 2006749. [[CrossRef](#)]
14. Da Silva, L.M.; Cesar, R.; Moreira, C.M.R.; Santos, J.H.M.; De Souza, L.G.; Pires, B.M.; Vicentini, R.; Nunes, W.; Zanin, H. Reviewing the fundamentals of supercapacitors and the difficulties involving the analysis of the electrochemical findings obtained for porous electrode materials. *Energy Storage Mater.* **2020**, *27*, 555–590. [[CrossRef](#)]
15. Lv, T.; Liu, M.; Zhu, D.; Gan, L.; Chen, T. Nanocarbon-Based Materials for Flexible All-Solid-State Supercapacitors. *Adv. Mater.* **2018**, *30*, 1705489. [[CrossRef](#)]
16. Wang, Y.; Zhang, L.; Hou, H.; Xu, W.; Duan, G.; He, S.; Liu, K.; Jiang, S. Recent progress in carbon-based materials for supercapacitor electrodes: A review. *J. Mater. Sci.* **2021**, *56*, 173–200. [[CrossRef](#)]
17. Duan, G.; Zhao, L.; Chen, L.; Wang, F.; He, S.; Jiang, S.; Zhang, Q. ZnCl_2 regulated flax-based porous carbon fibers for supercapacitors with good cycling stability. *New J. Chem.* **2021**, *45*, 22602–22609. [[CrossRef](#)]
18. Dai, L.; Chang, D.W.; Baek, J.-B.; Lu, W. Carbon Nanomaterials for Advanced Energy Conversion and Storage. *Small* **2012**, *8*, 1130–1166. [[CrossRef](#)] [[PubMed](#)]
19. Xu, T.; Du, H.; Liu, H.; Liu, W.; Zhang, X.; Si, C.; Liu, P.; Zhang, K. Advanced Nanocellulose-Based Composites for Flexible Functional Energy Storage Devices. *Adv. Mater.* **2021**, *33*, 2101368. [[CrossRef](#)]
20. Ariharan, A.; Ramesh, K.; Vinayagamoorthi, R.; Rani, M.S.; Viswanathan, B.; Ramaprabhu, S.; Nandhakumar, V. Biomass derived phosphorous containing porous carbon material for hydrogen storage and high-performance supercapacitor applications. *J. Energy Storage* **2021**, *35*, 102185. [[CrossRef](#)]
21. Fu, F.; Yang, D.; Fan, Y.; Qiu, X.; Huang, J.; Li, Z.; Zhang, W. Nitrogen-rich accordion-like lignin porous carbon via confined self-assembly template and in-situ mild activation strategy for high-performance supercapacitors. *J. Colloid Interface Sci.* **2022**, *628*, 90–99. [[CrossRef](#)]
22. Xiao, J.; Li, H.; Zhang, H.; He, S.; Zhang, Q.; Liu, K.; Jiang, S.; Duan, G.; Zhang, K. Nanocellulose and its derived composite electrodes toward supercapacitors: Fabrication, properties, and challenges. *J. Bioresour. Bioprod.* **2022**, *7*, 245–269. [[CrossRef](#)]
23. Guo, W.; Guo, X.; Yang, L.; Wang, T.; Zhang, M.; Duan, G.; Liu, X.; Li, Y. Synthetic melanin facilitates MnO supercapacitors with high specific capacitance and wide operation potential window. *Polymer* **2021**, *235*, 124276. [[CrossRef](#)]
24. Li, H.; Cao, L.; Zhang, H.; Tian, Z.; Zhang, Q.; Yang, F.; Yang, H.; He, S.; Jiang, S. Intertwined carbon networks derived from Polyimide/Cellulose composite as porous electrode for symmetrical supercapacitor. *J. Colloid Interface Sci.* **2022**, *609*, 179–187. [[CrossRef](#)]
25. Wei, L.; Deng, W.; Li, S.; Wu, Z.; Cai, J.; Luo, J. Sandwich-like chitosan porous carbon Spheres/MXene composite with high specific capacitance and rate performance for supercapacitors. *J. Bioresour. Bioprod.* **2022**, *7*, 63–72. [[CrossRef](#)]
26. Zheng, S.; Zhang, J.; Deng, H.; Du, Y.; Shi, X. Chitin derived nitrogen-doped porous carbons with ultrahigh specific surface area and tailored hierarchical porosity for high performance supercapacitors. *J. Bioresour. Bioprod.* **2021**, *6*, 142–151. [[CrossRef](#)]
27. Huang, J.; Zhao, B.; Liu, T.; Mou, J.; Jiang, Z.; Liu, J.; Li, H.; Liu, M. Wood-Derived Materials for Advanced Electrochemical Energy Storage Devices. *Adv. Funct. Mater.* **2019**, *29*, 1902255. [[CrossRef](#)]
28. Arjunan, A.; Kim, S.-K. Bioinspired Sustainable Sheetlike Porous Carbon Derived from Cassia fistula Flower Petal as an Electrode for High-Performance Supercapacitors. *Energy Fuels* **2022**, *36*, 9337–9346. [[CrossRef](#)]
29. Yang, J.; Li, H.; He, S.; Du, H.; Liu, K.; Zhang, C.; Jiang, S. Facile Electrodeposition of NiCo_2O_4 Nanosheets on Porous Carbonized Wood for Wood-Derived Asymmetric Supercapacitors. *Polymers* **2022**, *14*, 2521. [[CrossRef](#)]
30. Grądzka, E.; Wysocka-Żołopa, M.; Winkler, K. Fullerene-Based Conducting Polymers: N-Dopable Materials for Charge Storage Application. *Adv. Energy Mater.* **2020**, *10*, 2001443. [[CrossRef](#)]
31. Xu, T.; Shen, W.; Huang, W.; Lu, X. Fullerene micro/nanostructures: Controlled synthesis and energy applications. *Mater. Today Nano* **2020**, *11*, 100081. [[CrossRef](#)]
32. Chen, K.; Song, S.; Liu, F.; Xue, D. Structural design of graphene for use in electrochemical energy storage devices. *Chem. Soc. Rev.* **2015**, *44*, 6230–6257. [[CrossRef](#)]
33. Wu, Y.; Ma, B.; Cheng, S.; Liu, Y.; Chen, S.; Fu, J.; Xie, E. Three-dimensional micro/nano-interconnected scaffold graphene-based micro-supercapacitors with high electrochemical performance. *Electrochim. Acta* **2022**, *427*, 140864. [[CrossRef](#)]
34. Cao, L.; Li, H.; Liu, X.; Liu, S.; Zhang, L.; Xu, W.; Yang, H.; Hou, H.; He, S.; Zhao, Y.; et al. Nitrogen, sulfur co-doped hierarchical carbon encapsulated in graphene with “sphere-in-layer” interconnection for high-performance supercapacitor. *J. Colloid Interface Sci.* **2021**, *599*, 443–452. [[CrossRef](#)]
35. Yu, M.; Qiu, W.; Wang, F.; Zhai, T.; Fang, P.; Lu, X.; Tong, Y. Three dimensional architectures: Design, assembly and application in electrochemical capacitors. *J. Mater. Chem. A* **2015**, *3*, 15792–15823. [[CrossRef](#)]
36. Xu, Z.; Deng, W.; Wang, X. 3D Hierarchical Carbon-Rich Micro-/Nanomaterials for Energy Storage and Catalysis. *Electrochim. Energy Rev.* **2021**, *4*, 269–335. [[CrossRef](#)]
37. Mahmood, N.; De Castro, I.A.; Pramoda, K.; Khoshmanesh, K.; Bhargava, S.K.; Kalantar-Zadeh, K. Atomically thin two-dimensional metal oxide nanosheets and their heterostructures for energy storage. *Energy Storage Mater.* **2019**, *16*, 455–480. [[CrossRef](#)]
38. Dong, D. Ternary Composite $\text{MnO}_2@\text{MoS}_2/\text{Polypprrole}$ from In-situ Synthesis for Binder-free and Flexible Supercapacitor. *J. Bioresour. Bioprod.* **2019**, *4*, 242–250. [[CrossRef](#)]

39. Li, Q.; Zheng, S.; Xu, Y.; Xue, H.; Pang, H. Ruthenium based materials as electrode materials for supercapacitors. *Chem. Eng. J.* **2018**, *333*, 505–518. [[CrossRef](#)]
40. Wang, H.; Dai, H. Strongly coupled inorganic–nano-carbon hybrid materials for energy storage. *Chem. Soc. Rev.* **2013**, *42*, 3088–3113. [[CrossRef](#)]
41. Orangi, J.; Beidaghi, M. A Review of the Effects of Electrode Fabrication and Assembly Processes on the Structure and Electrochemical Performance of 2D MXenes. *Adv. Funct. Mater.* **2020**, *30*, 2005305. [[CrossRef](#)]
42. Lin, L.; Lei, W.; Zhang, S.; Liu, Y.; Wallace, G.G.; Chen, J. Two-dimensional transition metal dichalcogenides in supercapacitors and secondary batteries. *Energy Storage Mater.* **2019**, *19*, 408–423. [[CrossRef](#)]
43. Zhai, S.; Wei, L.; Karahan, H.E.; Chen, X.; Wang, C.; Zhang, X.; Chen, J.; Wang, X.; Chen, Y. 2D materials for 1D electrochemical energy storage devices. *Energy Storage Mater.* **2019**, *19*, 102–123. [[CrossRef](#)]
44. Hu, M.; Zhang, H.; Hu, T.; Fan, B.; Wang, X.; Li, Z. Emerging 2D MXenes for supercapacitors: Status, challenges and prospects. *Chem. Soc. Rev.* **2020**, *49*, 6666–6693. [[CrossRef](#)] [[PubMed](#)]
45. Li, X.; Du, D.; Zhang, Y.; Xing, W.; Xue, Q.; Yan, Z. Layered double hydroxides toward high-performance supercapacitors. *J. Mater. Chem. A* **2017**, *5*, 15460–15485. [[CrossRef](#)]
46. Ju, J.; Ma, J.; Wang, Y.; Cui, Y.; Han, P.; Cui, G. Solid-state energy storage devices based on two-dimensional nano-materials. *Energy Storage Mater.* **2019**, *20*, 269–290. [[CrossRef](#)]
47. Tang, Q.; Jiang, D.-E. Stabilization and Band-Gap Tuning of the 1T-MoS₂ Monolayer by Covalent Functionalization. *Chem. Mat.* **2015**, *27*, 3743–3748. [[CrossRef](#)]
48. Zhang, Y.; Ang, E.H.; Yang, Y.; Ye, M.; Du, W.; Li, C.C. Interlayer Chemistry of Layered Electrode Materials in Energy Storage Devices. *Adv. Funct. Mater.* **2021**, *31*, 2007358. [[CrossRef](#)]
49. Zhao, Z.; Xia, K.; Hou, Y.; Zhang, Q.; Ye, Z.; Lu, J. Designing flexible, smart and self-sustainable supercapacitors for portable/wearable electronics: From conductive polymers. *Chem. Soc. Rev.* **2021**, *50*, 12702–12743. [[CrossRef](#)]
50. Schon, T.B.; McAllister, B.T.; Li, P.-F.; Seferos, D.S. The rise of organic electrode materials for energy storage. *Chem. Soc. Rev.* **2016**, *45*, 6345–6404. [[CrossRef](#)] [[PubMed](#)]
51. Lima, R.M.A.P.; Alcaraz-Espinoza, J.J.; da Silva, F.A.G., Jr.; de Oliveira, H.P. Multifunctional Wearable Electronic Textiles Using Cotton Fibers with Polypyrrole and Carbon Nanotubes. *ACS Appl. Mater. Interfaces* **2018**, *10*, 13783–13795. [[CrossRef](#)]
52. Han, X.; Xiao, G.; Wang, Y.; Chen, X.; Duan, G.; Wu, Y.; Gong, X.; Wang, H. Design and fabrication of conductive polymer hydrogels and their applications in flexible supercapacitors. *J. Mater. Chem. A* **2020**, *8*, 23059–23095. [[CrossRef](#)]
53. Yang, H.; Lee, J.; Cheong, J.Y.; Wang, Y.; Duan, G.; Hou, H.; Jiang, S.; Kim, I.-D. Molecular engineering of carbonyl organic electrodes for rechargeable metal-ion batteries: Fundamentals, recent advances, and challenges. *Energy Environ. Sci.* **2021**, *14*, 4228–4267. [[CrossRef](#)]
54. Okhay, O.; Tkach, A. Polyaniline—Graphene Electrodes Prepared by Electropolymerization for High-Performance Capacitive Electrodes: A Brief Review. *Batteries* **2022**, *8*, 191. [[CrossRef](#)]
55. Liu, J.; Song, X.; Zhang, T.; Liu, S.; Wen, H.; Chen, L. 2D Conductive Metal–Organic Frameworks: An Emerging Platform for Electrochemical Energy Storage. *Angew. Chem.—Int. Ed.* **2021**, *60*, 5612–5624. [[CrossRef](#)] [[PubMed](#)]
56. Liu, X.; Shi, C.; Zhai, C.; Cheng, M.; Liu, Q.; Wang, G. Cobalt-Based Layered Metal–Organic Framework as an Ultrahigh Capacity Supercapacitor Electrode Material. *ACS Appl. Mater. Interfaces* **2016**, *8*, 4585–4591. [[CrossRef](#)]
57. Shao, D.; Wang, L.; Lu, B.; Guo, J.; Zhang, S.; Lu, Y. A high N content cobalt-based metal organic framework with nanorod structure for supercapacitor electrode material. *J. Electroanal. Chem.* **2019**, *847*, 113188. [[CrossRef](#)]
58. Sheberla, D.; Bachman, J.C.; Elias, J.S.; Sun, C.-J.; Shao-Horn, Y.; Dincă, M. Conductive MOF electrodes for stable supercapacitors with high areal capacitance. *Nat. Mater.* **2017**, *16*, 220–224. [[CrossRef](#)]
59. Sanati, S.; Abazari, R.; Albero, J.; Morsali, A.; García, H.; Liang, Z.; Zou, R. Metal–Organic Framework Derived Bimetallic Materials for Electrochemical Energy Storage. *Angew. Chem.—Int. Ed.* **2021**, *60*, 11048–11067. [[CrossRef](#)]
60. Li, M.; Liu, J.; Zhang, T.; Song, X.; Chen, W.; Chen, L. 2D Redox-Active Covalent Organic Frameworks for Supercapacitors: Design, Synthesis, and Challenges. *Small* **2021**, *17*, 2005073. [[CrossRef](#)]
61. Khattak, A.M.; Ghazi, Z.A.; Liang, B.; Khan, N.A.; Iqbal, A.; Li, L.; Tang, Z. A redox-active 2D covalent organic framework with pyridine moieties capable of faradaic energy storage. *J. Mater. Chem. A* **2016**, *4*, 16312–16317. [[CrossRef](#)]
62. DeBlase, C.R.; Hernández-Burgos, K.; Silberstein, K.E.; Rodriguez-Calero, G.G.; Bisbey, R.P.; Abruña, H.D.; Dichtel, W.R. Rapid and Efficient Redox Processes within 2D Covalent Organic Framework Thin Films. *ACS Nano* **2015**, *9*, 3178–3183. [[CrossRef](#)]
63. Xu, F.; Xu, H.; Chen, X.; Wu, D.; Wu, Y.; Liu, H.; Gu, C.; Fu, R.; Jiang, D. Radical Covalent Organic Frameworks: A General Strategy to Immobilize Open-Accessible Polyradicals for High-Performance Capacitive Energy Storage. *Angew. Chem.—Int. Ed.* **2015**, *54*, 6814–6818. [[CrossRef](#)] [[PubMed](#)]
64. Chen, H.; Ling, M.; Hencz, L.; Ling, H.Y.; Li, G.; Lin, Z.; Liu, G.; Zhang, S. Exploring Chemical, Mechanical, and Electrical Functionalities of Binders for Advanced Energy-Storage Devices. *Chem. Rev.* **2018**, *118*, 8936–8982. [[CrossRef](#)] [[PubMed](#)]
65. Zhong, S.; Zhan, C.; Cao, D. Zeolitic imidazolate framework-derived nitrogen-doped porous carbons as high performance supercapacitor electrode materials. *Carbon* **2015**, *85*, 51–59. [[CrossRef](#)]
66. Bresser, D.; Buchholz, D.; Moretti, A.; Varzi, A.; Passerini, S. Alternative binders for sustainable electrochemical energy storage—The transition to aqueous electrode processing and bio-derived polymers. *Energy Environ. Sci.* **2018**, *11*, 3096–3127. [[CrossRef](#)]

67. Zheng, Y.; Huang, X.; Chen, J.; Wu, K.; Wang, J.; Zhang, X. A Review of Conductive Carbon Materials for 3D Printing: Materials, Technologies, Properties, and Applications. *Materials* **2021**, *14*, 3911. [[CrossRef](#)]
68. Liu, L.; Zhao, H.; Lei, Y. Review on Nanoarchitected Current Collectors for Pseudocapacitors. *Small Methods* **2019**, *3*, 1800341. [[CrossRef](#)]
69. Abdisattar, A.; Yeleuov, M.; Daulbayev, C.; Askaruly, K.; Tolynbekov, A.; Taurbekov, A.; Prikhodko, N. Recent advances and challenges of current collectors for supercapacitors. *Electrochem. Commun.* **2022**, *142*, 107373. [[CrossRef](#)]
70. Brayek, M.; Jemni, M.A.; Driss, Z.; Kantchev, G.; Abid, M.S. Study of Spark-Ignition Engine Fueled with Hydrogen Produced by the Reaction Between Aluminum and Water in Presence of KOH. *Arab. J. Sci. Eng.* **2019**, *44*, 695–705. [[CrossRef](#)]
71. Liu, X.; Jung, H.-G.; Kim, S.-O.; Choi, H.-S.; Lee, S.; Moon, J.H.; Lee, J.K. Silicon/copper dome-patterned electrodes for high-performance hybrid supercapacitors. *Sci. Rep.* **2013**, *3*, 3183. [[CrossRef](#)]
72. Kuenzel, M.; Bresser, D.; Kim, G.-T.; Axmann, P.; Wohlfahrt-Mehrens, M.; Passerini, S. Unveiling and Amplifying the Benefits of Carbon-Coated Aluminum Current Collectors for Sustainable $\text{LiNi}_{0.5}\text{Mn}_{1.5}\text{O}_4$ Cathodes. *ACS Appl. Energy Mater.* **2020**, *3*, 218–230. [[CrossRef](#)]
73. Chiam, S.L.; Lim, H.N.; Hafiz, S.M.; Pandikumar, A.; Huang, N.M. Electrochemical Performance of Supercapacitor with Stacked Copper Foils Coated with Graphene Nanoplatelets. *Sci. Rep.* **2018**, *8*, 3093. [[CrossRef](#)] [[PubMed](#)]
74. Wen, Y.H.; Shao, L.; Zhao, P.C.; Wang, B.Y.; Cao, G.P.; Yang, Y.S. Carbon coated stainless steel mesh as a low-cost and corrosion-resistant current collector for aqueous rechargeable batteries. *J. Mater. Chem. A* **2017**, *5*, 15752–15758. [[CrossRef](#)]
75. Zhang, Y.-Z.; Wang, Y.; Cheng, T.; Lai, W.-Y.; Pang, H.; Huang, W. Flexible supercapacitors based on paper substrates: A new paradigm for low-cost energy storage. *Chem. Soc. Rev.* **2015**, *44*, 5181–5199. [[CrossRef](#)] [[PubMed](#)]
76. Josef, E.; Yan, R.; Guterman, R.; Oschatz, M. Electrospun Carbon Fibers Replace Metals as a Current Collector in Supercapacitors. *ACS Appl. Energy Mater.* **2019**, *2*, 5724–5733. [[CrossRef](#)]
77. Luo, P.; Huang, L. Carbon Paper as Current Collectors in Graphene Hydrogel Electrodes for High-Performance Supercapacitors. *Nanomaterials* **2020**, *10*, 746. [[CrossRef](#)]
78. Liu, Z.; Bai, S.; Liu, B.; Guo, P.; Lv, M.; Liu, D.; He, D. Interfacial modification of a lightweight carbon foam current collector for high-energy density Si/LCO lithium-ion batteries. *J. Mater. Chem. A* **2017**, *5*, 13168–13175. [[CrossRef](#)]
79. Cao, Z.; Zhang, J.; Ding, Y.; Li, Y.; Shi, M.; Yue, H.; Qiao, Y.; Yin, Y.; Yang, S. In situ synthesis of flexible elastic N-doped carbon foam as a carbon current collector and interlayer for high-performance lithium sulfur batteries. *J. Mater. Chem. A* **2016**, *4*, 8636–8644. [[CrossRef](#)]
80. Li, M.; Wang, C.; Chen, Z.; Xu, K.; Lu, J. New Concepts in Electrolytes. *Chem. Rev.* **2020**, *120*, 6783–6819. [[CrossRef](#)]
81. Xia, L.; Yu, L.; Hu, D.; Chen, G.Z. Electrolytes for electrochemical energy storage. *Mat. Chem. Front.* **2017**, *1*, 584–618. [[CrossRef](#)]
82. Peng, J.; Zhang, W.; Wang, S.; Huang, Y.; Wang, J.-Z.; Liu, H.-K.; Dou, S.-X.; Chou, S.-L. The Emerging Electrochemical Activation Tactic for Aqueous Energy Storage: Fundamentals, Applications, and Future. *Adv. Funct. Mater.* **2022**, *32*, 2111720. [[CrossRef](#)]
83. Zang, X.; Shen, C.; Sanghadasa, M.; Lin, L. High-Voltage Supercapacitors Based on Aqueous Electrolytes. *ChemElectroChem* **2019**, *6*, 976–988. [[CrossRef](#)]
84. Iqbal, M.Z.; Zakar, S.; Haider, S.S. Role of aqueous electrolytes on the performance of electrochemical energy storage device. *J. Electroanal. Chem.* **2020**, *858*, 113793. [[CrossRef](#)]
85. Nguyen, T.; Montemor, M.d.F. Metal Oxide and Hydroxide-Based Aqueous Supercapacitors: From Charge Storage Mechanisms and Functional Electrode Engineering to Need-Tailored Devices. *Adv. Sci.* **2019**, *6*, 1801797. [[CrossRef](#)]
86. Sajjad, M.; Khan, M.I.; Cheng, F.; Lu, W. A review on selection criteria of aqueous electrolytes performance evaluation for advanced asymmetric supercapacitors. *J. Energy Storage* **2021**, *40*, 102729. [[CrossRef](#)]
87. Krummacher, J.; Schütter, C.; Hess, L.H.; Balducci, A. Non-aqueous electrolytes for electrochemical capacitors. *Curr. Opin. Electrochem.* **2018**, *9*, 64–69. [[CrossRef](#)]
88. Simon, P.; Gogotsi, Y. Capacitive Energy Storage in Nanostructured Carbon–Electrolyte Systems. *Acc. Chem. Res.* **2013**, *46*, 1094–1103. [[CrossRef](#)] [[PubMed](#)]
89. Brandon, E.J.; Smart, M.C.; West, W.C. Low-temperature performance of electrochemical capacitors using acetonitrile/methyl formate electrolytes and activated carbon fabric electrodes. *J. Mater. Res.* **2020**, *35*, 113–121. [[CrossRef](#)]
90. Barthel, J.; Gores, H.-J.; Schmeer, G.; Wachter, R. Non-aqueous electrolyte solutions in chemistry and modern technology. In *Physical and Inorganic Chemistry*; Springer: Berlin/Heidelberg, Germany, 1983; pp. 33–144.
91. Lyklema, J. Principles of interactions in non-aqueous electrolyte solutions. *Curr. Opin. Colloid Interface Sci.* **2013**, *18*, 116–128. [[CrossRef](#)]
92. Ye, W.; Wang, H.; Ning, J.; Zhong, Y.; Hu, Y. New types of hybrid electrolytes for supercapacitors. *J. Energy Chem.* **2021**, *57*, 219–232. [[CrossRef](#)]
93. Venâncio, R.; Vicentini, R.; Costa, L.H.; Teófilo, R.; Da Silva, L.M.; Zanin, H. In-situ electrochemical and operando Raman techniques to investigate the effect of porosity in different carbon electrodes in organic electrolyte supercapacitors. *J. Energy Storage* **2022**, *50*, 104219. [[CrossRef](#)]
94. Wang, X.; Salari, M.; Jiang, D.-E.; Chapman Varela, J.; Anasori, B.; Wesolowski, D.J.; Dai, S.; Grinstaff, M.W.; Gogotsi, Y. Electrode material–ionic liquid coupling for electrochemical energy storage. *Nat. Rev. Mater.* **2020**, *5*, 787–808. [[CrossRef](#)]
95. Pan, S.; Yao, M.; Zhang, J.; Li, B.; Xing, C.; Song, X.; Su, P.; Zhang, H. Recognition of Ionic Liquids as High-Voltage Electrolytes for Supercapacitors. *Front. Chem.* **2020**, *8*, 261. [[CrossRef](#)] [[PubMed](#)]

96. Yu, L.; Chen, G.Z. Ionic Liquid-Based Electrolytes for Supercapacitor and Supercapattery. *Front. Chem.* **2019**, *7*, 272. [[CrossRef](#)] [[PubMed](#)]
97. Kim, E.; Han, J.; Ryu, S.; Choi, Y.; Yoo, J. Ionic Liquid Electrolytes for Electrochemical Energy Storage Devices. *Materials* **2021**, *14*, 4000. [[CrossRef](#)]
98. Tian, X.; Zhu, Q.; Xu, B. “Water-in-Salt” Electrolytes for Supercapacitors: A Review. *ChemSusChem* **2021**, *14*, 2501–2515. [[CrossRef](#)] [[PubMed](#)]
99. Lv, T.; Suo, L. Water-in-salt widens the electrochemical stability window: Thermodynamic and kinetic factors. *Curr. Opin. Electrochem.* **2021**, *29*, 100818. [[CrossRef](#)]
100. Santos, J.P.A.; Pinzón, M.J.; Santos, É.A.; Vicentini, R.; Pagan, C.J.B.; Da Silva, L.M.; Zanin, H. Boosting energy-storage capability in carbon-based supercapacitors using low-temperature water-in-salt electrolytes. *J. Energy Chem.* **2022**, *70*, 521–530. [[CrossRef](#)]
101. Suo, L.; Borodin, O.; Sun, W.; Fan, X.; Yang, C.; Wang, F.; Gao, T.; Ma, Z.; Schroeder, M.; von Cresce, A.; et al. Advanced High-Voltage Aqueous Lithium-Ion Battery Enabled by “Water-in-Bisalt” Electrolyte. *Angew. Chem.—Int. Ed.* **2016**, *55*, 7136–7141. [[CrossRef](#)] [[PubMed](#)]
102. Jiang, L.; Liu, L.; Yue, J.; Zhang, Q.; Zhou, A.; Borodin, O.; Suo, L.; Li, H.; Chen, L.; Xu, K.; et al. High-Voltage Aqueous Na-Ion Battery Enabled by Inert-Cation-Assisted Water-in-Salt Electrolyte. *Adv. Mater.* **2020**, *32*, 1904427. [[CrossRef](#)]
103. Wu, J.; Liang, Q.; Yu, X.; Lü, Q.-F.; Ma, L.; Qin, X.; Chen, G.; Li, B. Deep Eutectic Solvents for Boosting Electrochemical Energy Storage and Conversion: A Review and Perspective. *Adv. Funct. Mater.* **2021**, *31*, 2011102. [[CrossRef](#)]
104. Ge, X.; Gu, C.; Wang, X.; Tu, J. Deep eutectic solvents (DESs)-derived advanced functional materials for energy and environmental applications: Challenges, opportunities, and future vision. *J. Mater. Chem. A* **2017**, *5*, 8209–8229. [[CrossRef](#)]
105. Boisset, A.; Menne, S.; Jacquemin, J.; Balducci, A.; Anouti, M. Deep eutectic solvents based on N-methylacetamide and a lithium salt as suitable electrolytes for lithium-ion batteries. *Phys. Chem. Chem. Phys.* **2013**, *15*, 20054–20063. [[CrossRef](#)] [[PubMed](#)]
106. Zhao, J.; Zhang, J.; Yang, W.; Chen, B.; Zhao, Z.; Qiu, H.; Dong, S.; Zhou, X.; Cui, G.; Chen, L. “Water-in-deep eutectic solvent” electrolytes enable zinc metal anodes for rechargeable aqueous batteries. *Nano Energy* **2019**, *57*, 625–634. [[CrossRef](#)]
107. Yuan, B.; Wen, K.; Chen, D.; Liu, Y.; Dong, Y.; Feng, C.; Han, Y.; Han, J.; Zhang, Y.; Xia, C.; et al. Composite Separators for Robust High Rate Lithium Ion Batteries. *Adv. Funct. Mater.* **2021**, *31*, 2101420. [[CrossRef](#)]
108. Li, J.; Jia, H.; Ma, S.; Xie, L.; Wei, X.-X.; Dai, L.; Wang, H.; Su, F.; Chen, C.-M. Separator Design for High-Performance Supercapacitors: Requirements, Challenges, Strategies, and Prospects. *ACS Energy Lett.* **2023**, *8*, 56–78. [[CrossRef](#)]
109. Wang, X.; Chen, Y.; Schmidt, O.G.; Yan, C. Engineered nanomembranes for smart energy storage devices. *Chem. Soc. Rev.* **2016**, *45*, 1308–1330. [[CrossRef](#)]
110. Zhang, W.; Liu, H.; Zhang, X.; Li, X.; Zhang, G.; Cao, P. 3D Printed Micro-Electrochemical Energy Storage Devices: From Design to Integration. *Adv. Funct. Mater.* **2021**, *31*, 2104909. [[CrossRef](#)]
111. Bon, C.Y.; Mohammed, L.; Kim, S.; Manasi, M.; Isheunesu, P.; Lee, K.S.; Ko, J.M. Flexible poly(vinyl alcohol)-ceramic composite separators for supercapacitor applications. *J. Ind. Eng. Chem.* **2018**, *68*, 173–179. [[CrossRef](#)]
112. Liu, M.; Turchenik, K.; Fu, W.; Yang, Y.; Liu, M.; Yushin, G. Scalable, safe, high-rate supercapacitor separators based on the Al₂O₃ nanowire Polyvinyl butyral nonwoven membranes. *Nano Energy* **2020**, *71*, 104627. [[CrossRef](#)]
113. Torvinen, K.; Lehtimäki, S.; Keränen, J.T.; Sievänen, J.; Virtainen, J.; Hellén, E.; Lupo, D.; Tuukkanen, S. Pigment-cellulose nanofibril composite and its application as a separator-substrate in printed supercapacitors. *Electron. Mater. Lett.* **2015**, *11*, 1040–1047. [[CrossRef](#)]
114. Yang, D.; Qi, L.; Ma, J. Eggshell Membrane Templating of Hierarchically Ordered Macroporous Networks Composed of TiO₂ Tubes. *Adv. Mater.* **2002**, *14*, 1543–1546. [[CrossRef](#)]
115. Cai, J.; Liu, S.; Feng, J.; Kimura, S.; Wada, M.; Kuga, S.; Zhang, L. Cellulose–Silica Nanocomposite Aerogels by In Situ Formation of Silica in Cellulose Gel. *Angew. Chem.—Int. Ed.* **2012**, *51*, 2076–2079. [[CrossRef](#)] [[PubMed](#)]
116. Tammela, P.; Olsson, H.; Strømme, M.; Nyholm, L. The influence of electrode and separator thickness on the cell resistance of symmetric cellulose–polypyrrole-based electric energy storage devices. *J. Power Sources* **2014**, *272*, 468–475. [[CrossRef](#)]
117. Egorov, V.; Gulzar, U.; Zhang, Y.; Breen, S.; O’Dwyer, C. Evolution of 3D Printing Methods and Materials for Electrochemical Energy Storage. *Adv. Mater.* **2020**, *32*, 2000556. [[CrossRef](#)] [[PubMed](#)]
118. Baig, M.M.; Gul, I.H.; Baig, S.M.; Shahzad, F. The complementary advanced characterization and electrochemical techniques for electrode materials for supercapacitors. *J. Energy Storage* **2021**, *44*, 103370. [[CrossRef](#)]
119. Elgrishi, N.; Rountree, K.J.; McCarthy, B.D.; Rountree, E.S.; Eisenhart, T.T.; Dempsey, J.L. A Practical Beginner’s Guide to Cyclic Voltammetry. *J. Chem. Educ.* **2018**, *95*, 197–206. [[CrossRef](#)]
120. Zeng, L.; Wu, T.; Ye, T.; Mo, T.; Qiao, R.; Feng, G. Modeling galvanostatic charge–discharge of nanoporous supercapacitors. *Nat. Comp. Sci.* **2021**, *1*, 725–731. [[CrossRef](#)]
121. Kurzweil, P.; Shamonin, M. State-of-Charge Monitoring by Impedance Spectroscopy during Long-Term Self-Discharge of Supercapacitors and Lithium-Ion Batteries. *Batteries* **2018**, *4*, 35. [[CrossRef](#)]
122. Zhang, S.; Pan, N. Supercapacitors Performance Evaluation. *Adv. Energy Mater.* **2015**, *5*, 1401401. [[CrossRef](#)]
123. Bhide, A.; Hofmann, J.; Katharina Dürr, A.; Janek, J.; Adelhelm, P. Electrochemical stability of non-aqueous electrolytes for sodium-ion batteries and their compatibility with Na_{0.7}CoO₂. *Phys. Chem. Chem. Phys.* **2014**, *16*, 1987–1998. [[CrossRef](#)] [[PubMed](#)]
124. Forse, A.C.; Merlet, C.; Griffin, J.M.; Grey, C.P. New Perspectives on the Charging Mechanisms of Supercapacitors. *J. Am. Chem. Soc.* **2016**, *138*, 5731–5744. [[CrossRef](#)] [[PubMed](#)]

125. Simon, P.; Gogotsi, Y. Charge storage mechanism in nanoporous carbons and its consequence for electrical double layer capacitors. *Philos. Trans. R. Soc. A-Math. Phys. Eng. Sci.* **2010**, *368*, 3457–3467. [CrossRef] [PubMed]
126. Shao, H.; Wu, Y.-C.; Lin, Z.; Taberna, P.-L.; Simon, P. Nanoporous carbon for electrochemical capacitive energy storage. *Chem. Soc. Rev.* **2020**, *49*, 3005–3039. [CrossRef] [PubMed]
127. Wang, L.; Sun, J.; Zhang, H.; Xu, L.; Liu, G. Preparation of benzoxazine-based N-doped mesoporous carbon material and its electrochemical behaviour as supercapacitor. *J. Electroanal. Chem.* **2020**, *868*, 114196. [CrossRef]
128. Ferry, M.A.; Maruyama, J.; Asoh, T.-A.; Uyama, H. Porosity-Induced Improvement in KOH Activation of Chitin Nanofiber-Based Porous Carbon Leading to Ultrahigh Specific Capacitance. *ChemSusChem* **2022**, *15*, e202200932. [CrossRef]
129. Wu, Q.; Gao, M.; Jiang, C.; Gu, X.; Wang, Z.; Huang, L.; Yu, S. Carbon-carbon dense network composite with hierarchical structure for additive-free and high volumetric performance supercapacitor. *J. Power Sources* **2021**, *497*, 229878. [CrossRef]
130. Li, S.; Tian, Q.; Chen, J.; Chen, Y.; Guo, P.; Wei, C.; Cui, P.; Jiang, J.; Li, X.; Xu, Q. An intrinsically non-flammable organic electrolyte for wide temperature range supercapacitors. *Chem. Eng. J.* **2023**, *457*, 141265. [CrossRef]
131. Zhang, C.; Xie, Y.; Zhao, M.; Pentecost, A.E.; Ling, Z.; Wang, J.; Long, D.; Ling, L.; Qiao, W. Enhanced Electrochemical Performance of Hydrous RuO₂/Mesoporous Carbon Nanocomposites via Nitrogen Doping. *ACS Appl. Mater. Interfaces* **2014**, *6*, 9751–9759. [CrossRef]
132. Chen, G.Z. Linear and non-linear pseudocapacitances with or without diffusion control. *Prog. Nat. Sci.-Mater. Int.* **2021**, *31*, 792–800. [CrossRef]
133. Chen, G.Z. Supercapattery: Merit merge of capacitive and Nernstian charge storage mechanisms. *Curr. Opin. Electrochem.* **2020**, *21*, 358–367. [CrossRef]
134. Augustyn, V.; Simon, P.; Dunn, B. Pseudocapacitive oxide materials for high-rate electrochemical energy storage. *Energy Environ. Sci.* **2014**, *7*, 1597–1614. [CrossRef]
135. Chen, R.; Yu, M.; Sahu, R.P.; Puri, I.K.; Zhitomirsky, I. The Development of Pseudocapacitor Electrodes and Devices with High Active Mass Loading. *Adv. Energy Mater.* **2020**, *10*, 1903848. [CrossRef]
136. Fleischmann, S.; Mitchell, J.B.; Wang, R.; Zhan, C.; Jiang, D.-e.; Presser, V.; Augustyn, V. Pseudocapacitance: From Fundamental Understanding to High Power Energy Storage Materials. *Chem. Rev.* **2020**, *120*, 6738–6782. [CrossRef] [PubMed]
137. Eftekhari, A.; Mohamedi, M. Tailoring pseudocapacitive materials from a mechanistic perspective. *Mater. Today Energy* **2017**, *6*, 211–229. [CrossRef]
138. He, L.; Lin, C.; Zhao, Y.; Gao, W.; Zhang, H.; Lin, B.; Sun, D. A new strategy for porous carbon synthesis: Starch hydrogel as a carbon source for Co₃O₄@C supercapacitor electrodes. *Ceram. Int.* **2022**, *48*, 8104–8111. [CrossRef]
139. Hanlon, D.; Backes, C.; Higgins, T.M.; Hughes, M.; O'Neill, A.; King, P.; McEvoy, N.; Duesberg, G.S.; Mendoza Sanchez, B.; Pettersson, H.; et al. Production of Molybdenum Trioxide Nanosheets by Liquid Exfoliation and Their Application in High-Performance Supercapacitors. *Chem. Mat.* **2014**, *26*, 1751–1763. [CrossRef]
140. Pazhamalai, P.; Krishnamoorthy, K.; Manoharan, S.; Kim, S.J. High energy symmetric supercapacitor based on mechanically delaminated few-layered MoS₂ sheets in organic electrolyte. *J. Alloys Compd.* **2019**, *771*, 803–809. [CrossRef]
141. Seetha Lakshmi, K.C.; Ji, X.; Shao, L.-D.; Vedhanarayanan, B.; Lin, T.-W. Tailor-made organic polymers towards high voltage aqueous ammonium/potassium-ion asymmetric supercapacitors. *Appl. Surf. Sci.* **2022**, *577*, 151918. [CrossRef]
142. Lien, C.-W.; Vedhanarayanan, B.; Chen, J.-H.; Lin, J.-Y.; Tsai, H.-H.; Shao, L.-D.; Lin, T.-W. Optimization of acetonitrile/water content in hybrid deep eutectic solvent for graphene/MoS₂ hydrogel-based supercapacitors. *Chem. Eng. J.* **2021**, *405*, 126706. [CrossRef]
143. Tsai, H.-H.; Lin, T.-J.; Vedhanarayanan, B.; Tsai, C.-C.; Chen, T.-Y.; Ji, X.; Lin, T.-W. A 1.9-V all-organic battery-supercapacitor hybrid device with high rate capability and wide temperature tolerance in a metal-free water-in-saltelectrolyte. *J. Colloid Interface Sci.* **2022**, *612*, 76–87. [CrossRef]
144. Liu, H.; Liu, X.; Wang, S.; Liu, H.-K.; Li, L. Transition metal based battery-type electrodes in hybrid supercapacitors: A review. *Energy Storage Mater.* **2020**, *28*, 122–145. [CrossRef]
145. Shaikh, N.S.; Kanjanaboops, P.; Lokhande, V.C.; Praserthdam, S.; Lokhande, C.D.; Shaikh, J.S. Engineering of Battery Type Electrodes for High Performance Lithium Ion Hybrid Supercapacitors. *ChemElectroChem* **2021**, *8*, 4686–4724. [CrossRef]
146. Levi, M.D.; Lukatskaya, M.R.; Sigalov, S.; Beidaghi, M.; Shpigel, N.; Daikhin, L.; Aurbach, D.; Barsoum, M.W.; Gogotsi, Y. Solving the Capacitive Paradox of 2D MXene using Electrochemical Quartz-Crystal Admittance and In Situ Electronic Conductance Measurements. *Adv. Energy Mater.* **2015**, *5*, 1400815. [CrossRef]
147. Zhao, F.; Wang, Y.; Xu, X.; Liu, Y.; Song, R.; Lu, G.; Li, Y. Cobalt Hexacyanoferrate Nanoparticles as a High-Rate and Ultra-Stable Supercapacitor Electrode Material. *ACS Appl. Mater. Interfaces* **2014**, *6*, 11007–11012. [CrossRef]
148. Ji, J.; Zhang, L.L.; Ji, H.; Li, Y.; Zhao, X.; Bai, X.; Fan, X.; Zhang, F.; Ruoff, R.S. Nanoporous Ni(OH)₂ Thin Film on 3D Ultrathin-Graphite Foam for Asymmetric Supercapacitor. *ACS Nano* **2013**, *7*, 6237–6243. [CrossRef] [PubMed]
149. Dai, C.-S.; Chien, P.-Y.; Lin, J.-Y.; Chou, S.-W.; Wu, W.-K.; Li, P.-H.; Wu, K.-Y.; Lin, T.-W. Hierarchically Structured Ni₃S₂/Carbon Nanotube Composites as High Performance Cathode Materials for Asymmetric Supercapacitors. *ACS Appl. Mater. Interfaces* **2013**, *5*, 12168–12174. [CrossRef]
150. Wang, X.; Li, M.; Chang, Z.; Wang, Y.; Chen, B.; Zhang, L.; Wu, Y. Orientated Co₃O₄ Nanocrystals on MWCNTs as Superior Battery-Type Positive Electrode Material for a Hybrid Capacitor. *J. Electrochem. Soc.* **2015**, *162*, A1966. [CrossRef]

151. Chen, T.-Y.; Vedhanarayanan, B.; Lin, S.-Y.; Shao, L.-D.; Sofer, Z.; Lin, J.-Y.; Lin, T.-W. Electrodeposited NiSe on a forest of carbon nanotubes as a free-standing electrode for hybrid supercapacitors and overall water splitting. *J. Colloid Interface Sci.* **2020**, *574*, 300–311. [[CrossRef](#)]
152. Lakshmi, K.C.S.; Ji, X.; Chen, T.-Y.; Vedhanarayanan, B.; Lin, T.-W. Pseudocapacitive and battery-type organic polymer electrodes for a 1.9 V hybrid supercapacitor with a record concentration of ammonium acetate. *J. Power Sources* **2021**, *511*, 230434. [[CrossRef](#)]
153. Xie, J.; Yang, P.; Wang, Y.; Qi, T.; Lei, Y.; Li, C.M. Puzzles and confusions in supercapacitor and battery: Theory and solutions. *J. Power Sources* **2018**, *401*, 213–223. [[CrossRef](#)]
154. Zhang, P.; Wang, F.; Yu, M.; Zhuang, X.; Feng, X. Two-dimensional materials for miniaturized energy storage devices: From individual devices to smart integrated systems. *Chem. Soc. Rev.* **2018**, *47*, 7426–7451. [[CrossRef](#)] [[PubMed](#)]
155. Sumboja, A.; Liu, J.; Zheng, W.G.; Zong, Y.; Zhang, H.; Liu, Z. Electrochemical energy storage devices for wearable technology: A rationale for materials selection and cell design. *Chem. Soc. Rev.* **2018**, *47*, 5919–5945. [[CrossRef](#)]
156. Wang, L.; Fu, X.; He, J.; Shi, X.; Chen, T.; Chen, P.; Wang, B.; Peng, H. Application Challenges in Fiber and Textile Electronics. *Adv. Mater.* **2020**, *32*, 1901971. [[CrossRef](#)]
157. Chae, J.S.; Park, S.K.; Roh, K.C.; Park, H.S. Electrode materials for biomedical patchable and implantable energy storage devices. *Energy Storage Mater.* **2020**, *24*, 113–128. [[CrossRef](#)]
158. Meng, F.; Li, Q.; Zheng, L. Flexible fiber-shaped supercapacitors: Design, fabrication, and multi-functionalities. *Energy Storage Mater.* **2017**, *8*, 85–109. [[CrossRef](#)]
159. Cavallo, A.; Russo, A.; Caciello, G. Control of Supercapacitors for smooth EMA Operations in Aeronautical Applications. In Proceedings of the 2019 American Control Conference (ACC), Philadelphia, PA, USA, 10–12 July 2019; pp. 4948–4954.
160. Sumsurooah, S.; He, Y.; Torchio, M.; Kouramas, K.; Guida, B.; Cuomo, F.; Atkin, J.; Bozhko, S.; Renzetti, A.; Russo, A.; et al. ENIGMA—A Centralised Supervisory Controller for Enhanced Onboard Electrical Energy Management with Model in the Loop Demonstration. *Energies* **2021**, *14*, 5518. [[CrossRef](#)]
161. Wang, X.; Lu, X.; Liu, B.; Chen, D.; Tong, Y.; Shen, G. Flexible Energy-Storage Devices: Design Consideration and Recent Progress. *Adv. Mater.* **2014**, *26*, 4763–4782. [[CrossRef](#)] [[PubMed](#)]
162. Mackanic, D.G.; Chang, T.-H.; Huang, Z.; Cui, Y.; Bao, Z. Stretchable electrochemical energy storage devices. *Chem. Soc. Rev.* **2020**, *49*, 4466–4495. [[CrossRef](#)] [[PubMed](#)]
163. Wang, K.; Meng, Q.; Zhang, Y.; Wei, Z.; Miao, M. High-Performance Two-Ply Yarn Supercapacitors Based on Carbon Nanotubes and Polyaniline Nanowire Arrays. *Adv. Mater.* **2013**, *25*, 1494–1498. [[CrossRef](#)]
164. Lee, H.; Yoo, J.-K.; Park, J.-H.; Kim, J.H.; Kang, K.; Jung, Y.S. A Stretchable Polymer–Carbon Nanotube Composite Electrode for Flexible Lithium-Ion Batteries: Porosity Engineering by Controlled Phase Separation. *Adv. Energy Mater.* **2012**, *2*, 976–982. [[CrossRef](#)]
165. Hao, G.-P.; Hippauf, F.; Oschatz, M.; Wisser, F.M.; Leifert, A.; Nickel, W.; Mohamed-Noriega, N.; Zheng, Z.; Kaskel, S. Stretchable and Semitransparent Conductive Hybrid Hydrogels for Flexible Supercapacitors. *ACS Nano* **2014**, *8*, 7138–7146. [[CrossRef](#)] [[PubMed](#)]
166. Li, H.; Lv, T.; Sun, H.; Qian, G.; Li, N.; Yao, Y.; Chen, T. Ultrastretchable and superior healable supercapacitors based on a double cross-linked hydrogel electrolyte. *Nat. Commun.* **2019**, *10*, 536. [[CrossRef](#)]
167. Huang, Y.; Zhong, M.; Shi, F.; Liu, X.; Tang, Z.; Wang, Y.; Huang, Y.; Hou, H.; Xie, X.; Zhi, C. An Intrinsically Stretchable and Compressible Supercapacitor Containing a Polyacrylamide Hydrogel Electrolyte. *Angew. Chem.-Int. Ed.* **2017**, *56*, 9141–9145. [[CrossRef](#)]
168. Chen, X.; Villa, N.S.; Zhuang, Y.; Chen, L.; Wang, T.; Li, Z.; Kong, T. Stretchable Supercapacitors as Emergent Energy Storage Units for Health Monitoring Bioelectronics. *Adv. Energy Mater.* **2020**, *10*, 1902769. [[CrossRef](#)]
169. Gong, J.P. Materials both Tough and Soft. *Science* **2014**, *344*, 161–162. [[CrossRef](#)] [[PubMed](#)]
170. Song, C.; Yun, J.; Keum, K.; Jeong, Y.R.; Park, H.; Lee, H.; Lee, G.; Oh, S.Y.; Ha, J.S. High performance wire-type supercapacitor with Ppy/CNT-ionic liquid/AuNP/carbon fiber electrode and ionic liquid based electrolyte. *Carbon* **2019**, *144*, 639–648. [[CrossRef](#)]
171. Keum, K.; Lee, G.; Lee, H.; Yun, J.; Park, H.; Hong, S.Y.; Song, C.; Kim, J.W.; Ha, J.S. Wire-Shaped Supercapacitors with Organic Electrolytes Fabricated via Layer-by-Layer Assembly. *ACS Appl. Mater. Interfaces* **2018**, *10*, 26248–26257. [[CrossRef](#)]
172. Guo, Y.; Li, W.; Yu, H.; Perepichka, D.F.; Meng, H. Flexible Asymmetric Supercapacitors via Spray Coating of a New Electrochromic Donor–Acceptor Polymer. *Adv. Energy Mater.* **2017**, *7*, 1601623. [[CrossRef](#)]
173. Liu, Y.-Z.; Yao, W.; Gan, H.-M.; Sun, C.-Y.; Su, Z.-M.; Wang, X.-L. Polyoxometalates-Based Metal–Organic Frameworks Made by Electrodeposition and Carbonization Methods as Cathodes and Anodes for Asymmetric Supercapacitors. *Chem.—Eur. J.* **2019**, *25*, 16617–16624. [[CrossRef](#)]
174. Lv, Z.; Luo, Y.; Tang, Y.; Wei, J.; Zhu, Z.; Zhou, X.; Li, W.; Zeng, Y.; Zhang, W.; Zhang, Y.; et al. Editable Supercapacitors with Customizable Stretchability Based on Mechanically Strengthened Ultralong MnO₂ Nanowire Composite. *Adv. Mater.* **2018**, *30*, 1704531. [[CrossRef](#)]
175. Jiao, S.; Zhou, A.; Wu, M.; Hu, H. Kirigami Patterning of MXene/Bacterial Cellulose Composite Paper for All-Solid-State Stretchable Micro-Supercapacitor Arrays. *Adv. Sci.* **2019**, *6*, 1900529. [[CrossRef](#)]
176. Wang, H.; Zhu, B.; Jiang, W.; Yang, Y.; Leow, W.R.; Wang, H.; Chen, X. A Mechanically and Electrically Self-Healing Supercapacitor. *Adv. Mater.* **2014**, *26*, 3638–3643. [[CrossRef](#)] [[PubMed](#)]

177. Liu, F.; Wang, J.; Pan, Q. An all-in-one self-healable capacitor with superior performance. *J. Mater. Chem. A* **2018**, *6*, 2500–2506. [[CrossRef](#)]
178. Mai, W.; Yu, Q.; Han, C.; Kang, F.; Li, B. Self-Healing Materials for Energy-Storage Devices. *Adv. Funct. Mater.* **2020**, *30*, 1909912. [[CrossRef](#)]
179. Son, D.; Kang, J.; Vardoulis, O.; Kim, Y.; Matsuhisa, N.; Oh, J.Y.; To, J.W.F.; Mun, J.; Katsumata, T.; Liu, Y.; et al. An integrated self-healable electronic skin system fabricated via dynamic reconstruction of a nanostructured conducting network. *Nat. Nanotechnol.* **2018**, *13*, 1057–1065. [[CrossRef](#)] [[PubMed](#)]
180. Cao, Y.; Tan, Y.J.; Li, S.; Lee, W.W.; Guo, H.; Cai, Y.; Wang, C.; Tee, B.C.K. Self-healing electronic skins for aquatic environments. *Nat. Electron.* **2019**, *2*, 75–82. [[CrossRef](#)]
181. White, S.R.; Sottos, N.R.; Geubelle, P.H.; Moore, J.S.; Kessler, M.R.; Sriram, S.R.; Brown, E.N.; Viswanathan, S. Autonomic healing of polymer composites. *Nature* **2001**, *409*, 794–797. [[CrossRef](#)] [[PubMed](#)]
182. Park, S.; Thangavel, G.; Parida, K.; Li, S.; Lee, P.S. A Stretchable and Self-Healing Energy Storage Device Based on Mechanically and Electrically Restorative Liquid-Metal Particles and Carboxylated Polyurethane Composites. *Adv. Mater.* **2019**, *31*, 1805536. [[CrossRef](#)]
183. Liu, R.; Wang, Z.L.; Fukuda, K.; Someya, T. Flexible self-charging power sources. *Nat. Rev. Mater.* **2022**, *7*, 870–886. [[CrossRef](#)]
184. Luo, J.; Wang, Z.L. Recent advances in triboelectric nanogenerator based self-charging power systems. *Energy Storage Mater.* **2019**, *23*, 617–628. [[CrossRef](#)]
185. Mi, Y.; Lu, Y.; Wang, X.; Zhao, Z.; Cao, X.; Wang, N. From Triboelectric Nanogenerator to Uninterrupted Power Supply System: The Key Role of Electrochemical Batteries and Supercapacitors. *Batteries* **2022**, *8*, 215. [[CrossRef](#)]
186. Song, R.; Jin, H.; Li, X.; Fei, L.; Zhao, Y.; Huang, H.; Lai-Wa Chan, H.; Wang, Y.; Chai, Y. A rectification-free piezo-supercapacitor with a polyvinylidene fluoride separator and functionalized carbon cloth electrodes. *J. Mater. Chem. A* **2015**, *3*, 14963–14970. [[CrossRef](#)]
187. Pazhamalai, P.; Krishnamoorthy, K.; Mariappan, V.K.; Sahoo, S.; Manoharan, S.; Kim, S.-J. A High Efficacy Self-Charging MoSe₂ Solid-State Supercapacitor Using Electrospun Nanofibrous Piezoelectric Separator with Ionogel Electrolyte. *Adv. Mater. Interfaces* **2018**, *5*, 1800055. [[CrossRef](#)]
188. Zhao, D.; Wang, H.; Khan, Z.U.; Chen, J.C.; Gabrielsson, R.; Jonsson, M.P.; Berggren, M.; Crispin, X. Ionic thermoelectric supercapacitors. *Energy Environ. Sci.* **2016**, *9*, 1450–1457. [[CrossRef](#)]

Disclaimer/Publisher’s Note: The statements, opinions and data contained in all publications are solely those of the individual author(s) and contributor(s) and not of MDPI and/or the editor(s). MDPI and/or the editor(s) disclaim responsibility for any injury to people or property resulting from any ideas, methods, instructions or products referred to in the content.